Article

Crystal structures of agonist-bound human cannabinoid receptor CB_1

https://doi.org/10.1038/s41586-025-09454-5

Received: 13 May 2025

Accepted: 24 July 2025

Published online: 27 August 2025

Check for updates

Tian Hua[1,2,3], Kiran Vemuri[4,5,12], Spyros P. Nikas[4,5,12], Yiran Wu[1], Lu Qu[1,2,3], Mengchen Pu[1], Anisha Korde[4,5], Shan Jiang[4,5], Jo-Hao Ho[6], Gye Won Han[7,8], Kang Ding[1,3,9], Xuanxuan Li[10], Haiguang Liu[10], Michael A. Hanson[11], Suwen Zhao[1,9]✉, Laura M. Bohn[6]✉, Alexandros Makriyannis[4,5]✉, Raymond C. Stevens[1,7,8,9] & Zhi-Jie Liu[1,2,9]✉

Cannabinoid receptor 1 (CB_1) is the primary target of the partial agonist Δ^9-tetrahydrocannabinol (Δ^9-THC), the psychoactive constituent of marijuana[1]. Here we report two agonist-bound crystal structures of human CB_1 in complex with a tetrahydrocannabinol (AM11542) and a hexahydrocannabinol (AM841). The two CB_1–agonist complexes reveal important conformational changes in the overall structure relative to the antagonist-bound state[2], including a 53% reduction in the volume of the ligand-binding pocket and an increase in the surface area of the G protein-binding region. Furthermore, a twin toggle switch of $Phe200^{3.36}$ and $Trp356^{6.48}$ (where the superscripts denote Ballesteros–Weinstein numbering[3]) is experimentally observed and seems to be essential for receptor activation. The structures reveal important insights into the activation mechanism of CB_1 and provide a molecular basis for predicting the binding modes of Δ^9-THC, and endogenous and synthetic cannabinoids. The plasticity of the binding pocket of CB_1 seems to be a common feature among certain class A G protein-coupled receptors. These findings should inspire the design of chemically diverse ligands with distinct pharmacological properties.

Cannabis sativa L., commonly known as marijuana, has been used for medicinal and recreational purposes across different cultures for more than 5,000 years[4,5]. The principal *Cannabis* constituent, Δ^9-THC, exerts its psychotropic effects by activating CB_1, which is also the primary target of the endocannabinoids, anandamide (AEA) and 2-arachidonoyl glycerol (2-AG)[1,6]. Structural examination of CB_1 in complex with the AM6538 antagonist[2] and taranabant[7] provides molecular insights into the inactive state of the receptor, yet does not inform us as to how CB_1 elicits its diverse physiological effects.

To facilitate CB_1 crystallization in its agonist-bound form, two potent CB_1 agonists, AM11542 and AM841, were designed with specific structural features: a tricyclic terpenoid ring system; 6a*R* and 10a*R* stereochemistry at the junction of the B- and C-rings; and a phenolic hydroxyl group at C1—all of which also characterize the Δ^9-THC tricyclic ring system (Fig. 1a, Methods and Extended Data Fig. 1). The two ligands used in this study differ from Δ^9-THC by possessing a pivotal 1′,1′-gem-dimethylheptyl alkyl chain at the C3 position, as well as bromo and isothiocyanato groups as ω-substituents for AM11542 and AM841, respectively (Fig. 1a). Having high affinity for CB_1 and binding in a wash-resistant manner to the receptor (Fig. 1a–c), both AM11542 and AM841 are potent, full agonists of CB_1, as determined by their ability to inhibit forskolin-stimulated accumulation of cAMP compared with CP55,940. By contrast, Δ^9-THC acts as a partial agonist in this assay (Fig. 1d).

The two agonist-bound CB_1 structures were determined using a thermostabilizing construct as previously described[2] for CB_1–AM6538 (Extended Data Table 1 and Extended Data Fig. 2). The receptor conformations of the AM11542- and AM841-bound complexes are very similar (C_α root mean square deviation (r.m.s.d.) = 0.66 Å), and both ligands overlay well in the same binding pocket (Fig. 2a and Extended Data Fig. 3a). We therefore focus our discussions mainly on the higher-resolution CB_1–AM11542 structure (2.8 Å), while mentioning the specific differences of the AM841-bound complex (2.95 Å) where relevant. In contrast to a V-shaped loop in the CB_1–AM6538 structure, the truncated N terminus resides over the ligand-binding pocket where it is not directly involved in agonist binding (Fig. 2b), although this does not preclude the possibility that there may be conformational changes in a full-length N-terminal domain. A cholesterol molecule, which is absent in the antagonist-bound structure, is observed between the cytoplasmic portion of helices II, III and IV in the agonist-bound complexes (Extended Data Fig. 3b). This cholesterol binding cavity is revealed through a rotation of helix II coupled with conformational changes of the side chain of $Leu165^{2.52}$ (where the superscript denotes Ballesteros–Weinstein numbering[3]).

The agonist AM11542 adopts an L-shaped conformation in the orthosteric binding pocket, which is much smaller than the more expanded binding domain in the antagonist AM6538-bound structure (Fig. 2b–d). The interactions between AM11542 and CB_1 are mainly

[1]iHuman Institute, ShanghaiTech University, Shanghai, China. [2]National Laboratory of Biomacromolecules, Institute of Biophysics, Chinese Academy of Sciences, Beijing, China. [3]University of Chinese Academy of Sciences, Beijing, China. [4]Center for Drug Discovery, Department of Pharmaceutical Sciences, Northeastern University, Boston, MA, USA. [5]Department of Chemistry and Chemical Biology, Northeastern University, Boston, MA, USA. [6]Department of Molecular Medicine, The Scripps Research Institute, Jupiter, FL, USA. [7]Bridge Institute, University of Southern California, Los Angeles, CA, USA. [8]Department of Chemistry, University of Southern California, Los Angeles, CA, USA. [9]School of Life Science and Technology, ShanghaiTech University, Shanghai, China. [10]Complex Systems Division, Beijing Computational Science Research Center, Beijing, China. [11]GPCR Consortium, San Marcos, CA, USA. [12]These authors contributed equally: Kiran Vemuri, Spyros P. Nikas. ✉e-mail: zhaosw@shanghaitech.edu.cn; Laura.bohn@ufl.edu; a.makriyannis@neu.edu; liuzhj@shanghaitech.edu.cn

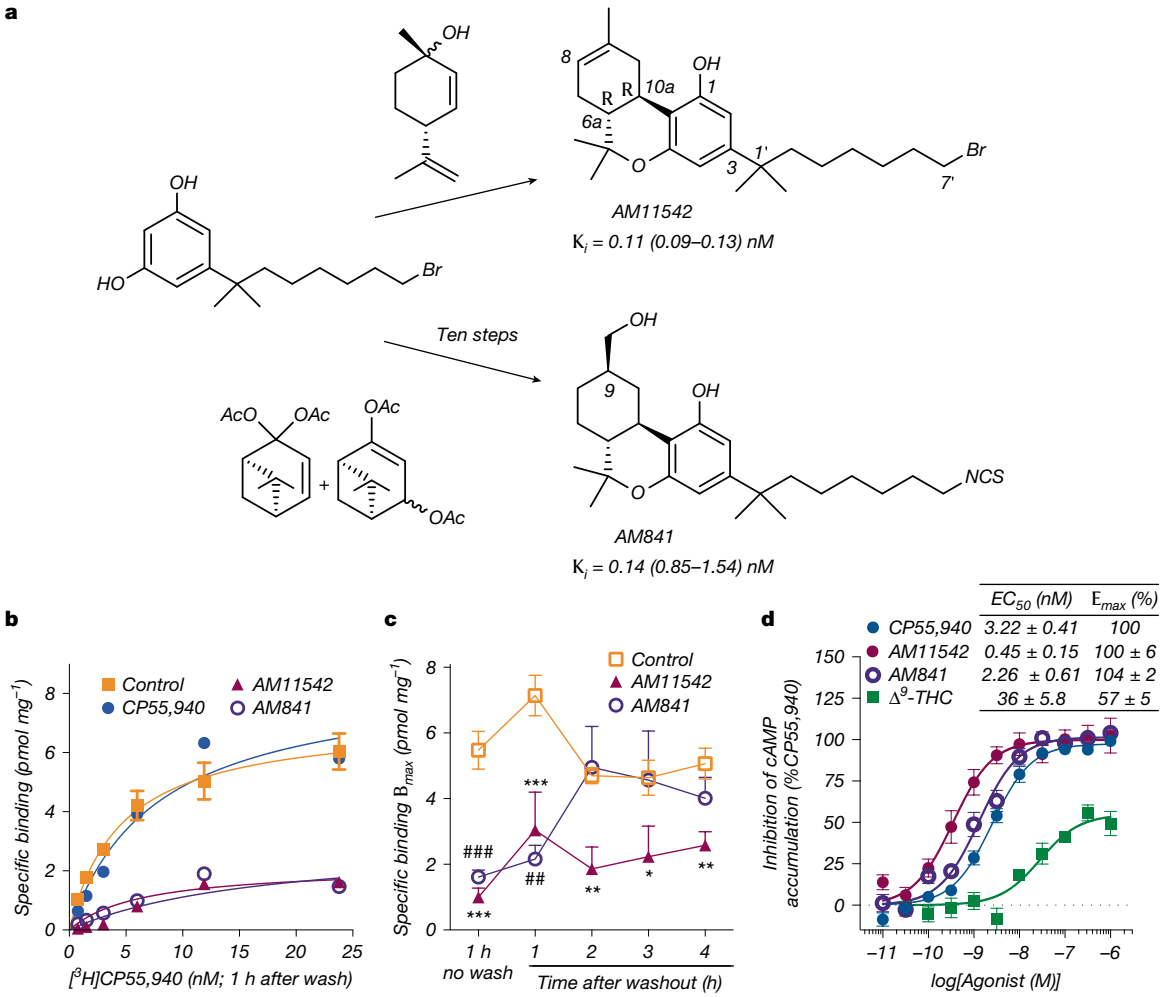

Fig. 1 | Synthesis and pharmacological characterization of AM11542 and AM841. a, Synthesis of AM11542 and AM841 (Extended Data Fig. 1) with radioligand binding affinity against [^{3}H]CP55,940. K_i, inhibition constant. **b**, Cell membranes were pretreated with CP55,940 (4 nM), AM11542 (1 nM), AM841 (10 nM) or buffer (control) for 1 h, washed and then subjected to [^{3}H]CP55,940 binding for 1 h. **c**, Maximal binding capacity (B_{max}) values were calculated from **b** and in experiments in which the incubation time of the radioligand was increased after the washing. Pretreatment with either AM11542 or AM841 prevents radioligand binding after 1 h incubation (control versus AM841, $^{\#\#}P < 0.01$; versus AM11542, $^{***}P < 0.001$), whereas AM11542 prevents radioligand binding at all later time points tested (control versus AM11542, $^{*}P < 0.05$, $^{**}P < 0.01$). Displacement of [^{3}H]CP55,940 binding in the presence of AM11542 (versus control, $^{***}P < 0.001$) and AM841 (versus control, $^{\#\#\#}P < 0.001$) is shown for comparison. Student's *t*-test versus control at each time point. Data are mean ± s.e.m., $n = 3$–6. **d**, Agonist activity measured as the inhibition of forskolin-stimulated cAMP accumulation. Data are mean ± s.e.m., $n \geq 6$ independent experiments. E_{max}, percentage of maximum response; EC_{50}, half-maximum effective concentration.

hydrophobic and aromatic, consisting of residues from extracellular loop 2 (ECL2) and helices III, V, VI and VII (Fig. 3a,d). The tricyclic tetrahydrocannabinol ring system of AM11542 forms π–π interactions with Phe268^{ECL2}, Phe379$^{7.35}$, Phe189$^{3.25}$ and Phe177$^{2.64}$, and the phenolic hydroxyl at C1 forms a hydrogen bond with Ser383$^{7.39}$. In agreement, substitution of Ser383$^{7.39}$Ala greatly reduces the CB_1 agonist potency of cannabinoid-like agonists such as AM11542, AM841 and CP55,940 (Fig. 3c, Extended Data Table 2 and Extended Data Fig. 4b). Notably, the hydroxyl group at the C11 position of AM841 forms an additional hydrogen bond with Ile267^{ECL2}.

The alkyl chain of the agonist extends into the long channel formed by helices III, V and VI, undergoing hydrophobic interactions with Leu193$^{3.29}$, Val196$^{3.32}$, Tyr275$^{5.39}$, Leu276$^{5.40}$, L359$^{6.51}$ and Met363$^{6.55}$ (Fig. 3a,d). Furthermore, the isothiocyanate moiety of AM841 forms a hydrogen bond with Tyr275$^{5.39}$. Notably, Tyr275$^{5.39}$Ala substitutions markedly decrease the potency of the agonists (Fig. 3c, Extended Data Table 2 and Extended Data Fig. 4b). Structure–activity relationship studies with classical cannabinoids have shown that the C3 alkyl chain lengths and *ω*-substitutions modulate ligand affinity. Furthermore, incorporation of a C1′-gem-dimethyl group affects the conformational properties of the alkyl chain and leads to notable enhancement in potency and efficacy[8–11]. Unlike Δ^9-THC, which has a shorter alkyl chain (*n*-pentyl), our results show that longer alkyl chains coupled with a C1′-gem-dimethyl group allow extended interactions with CB_1. Specifically, the C1′-gem-dimethyl group forms hydrophobic interactions with Phe200$^{3.36}$, Leu359$^{6.51}$ and Met363$^{6.55}$ (Fig. 3a,d). Taken together, these data provide important insights into the key role of the 1′,1′-gem-dimethylheptyl moiety in activating CB_1.

On the basis of the AM11542-bound CB_1 structure and mutagenesis data[12], we investigated the interactions of representative agonists from three different scaffolds (classical cannabinoids, endocannabinoids and aminoalkylindoles) with CB_1 through docking and molecular dynamics validation (Fig. 3e,f and Extended Data Fig. 5). The predicted binding mode of the classical cannabinoids Δ^9-THC (Fig. 3e) and HU-210 (Extended Data Fig. 5g) resembles that of AM11542 in the CB_1 crystal structure. HU-211—the enantiomer of HU-210—does not activate CB_1 (refs. 13,14) as it exhibits severe clashes when superimposed with its active enantiomer HU-210 (Extended Data Fig. 5i).

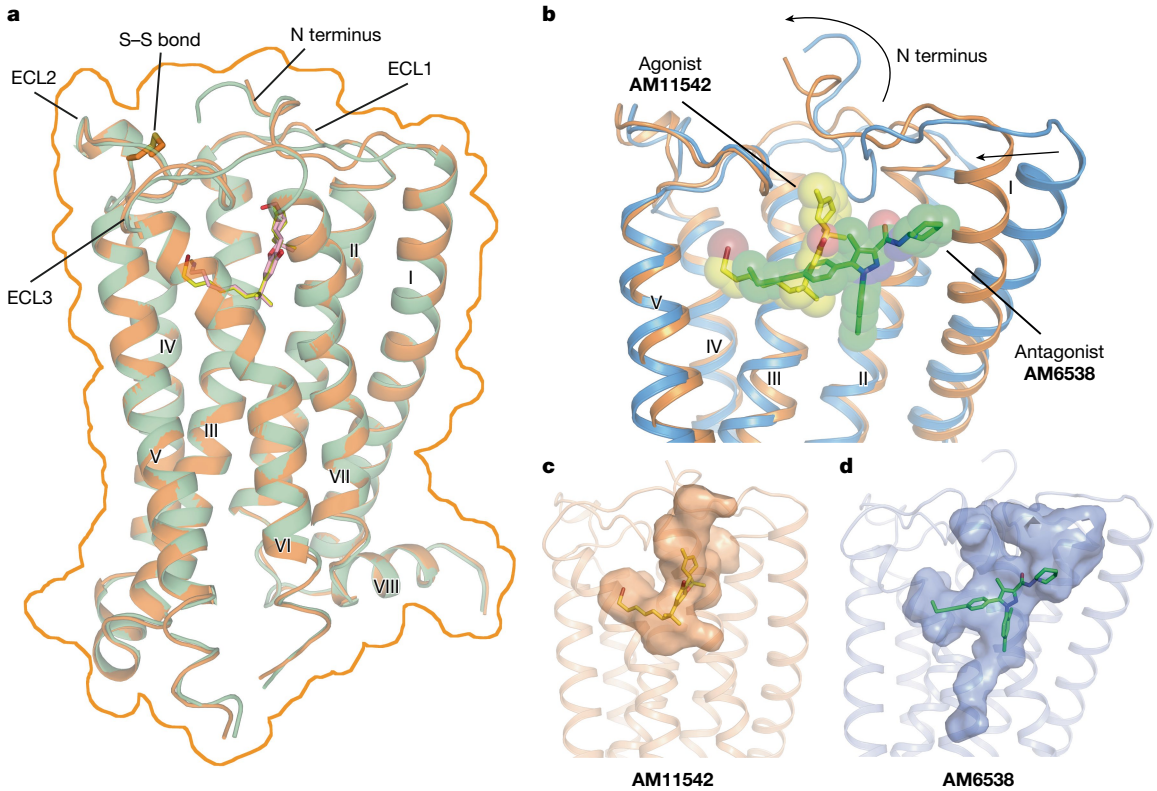

Fig. 2 | Overall structures of CB_1–AM11542 and CB_1–AM841 complexes. **a**, Superposition of the CB_1–AM11542 and CB_1–AM841 structures, with the surface outlined by an orange line. CB_1 is shown in orange and green along with ligands AM11542 (yellow sticks) and AM841 (pink sticks). **b**, Comparison of agonist-bound (orange) and antagonist-bound (blue) CB_1 ligand-binding pockets. AM11542 (yellow) and AM6538 (green) are shown as sticks and spheres. **c**,**d**, The shape of AM11542 (**c**) and AM6538 (**d**) binding pockets are shown as a surface representation.

The endocannabinoids AEA (Fig. 3f) and 2-AG (Extended Data Fig. 5j) adopt a C-shaped conformation and their long tails extend into the long channel. Compared with other lipid receptors such as sphingosine-1-phosphate receptor 1 ($S1P_1$), the alkyl chains of AM11542 and AM841 occupy a similar position to 'arm 2' of the antagonist AM6538 (ref. 2), as well as the alkyl chain of ML056 in the $S1P_1$ receptor[15] (Fig. 3b), indicating that this could be a conserved binding pocket for alkyl chains in lipid-binding receptors. The structurally distinct aminoalkylindoles WIN 55,212-2 (Extended Data Fig. 5k) and JWH-018 (Extended Data Fig. 5h) occupy the same position in the pocket as do AM11542 and AM841, exhibiting major π–π interactions with aromatic residues instead of the hydrogen-bond interactions observed in most classical cannabinoid–CB_1 interactions.

Comparisons between the agonist- and antagonist-bound CB_1 complexes reveal marked structural rearrangements (C_α r.m.s.d. of the overall structure without fusion protein = 3.52 Å; Fig. 4a). Compared with AM6538-bound CB_1, a notable conformational change occurs in helices I and II. The extracellular part of helix I bends inwards by 6.6 Å, whereas helix II rotates in by about 6.8 Å, respectively, in the AM11542-bound structure (Fig. 4b). Similarly, important conformational changes are also observed in the cytoplasmic part of the receptor, in which helix VI moves outwards by about 8 Å (Fig. 4b), resembling the β_2 adrenergic receptor (β_2AR)–G_s complex[16]. This is the largest structural change—especially in the extracellular portion—observed in the solved agonist- and antagonist-bound pairs of class A G protein-coupled receptors (GPCRs) (Extended Data Table 3). Therefore, owing to the inward shifts of helices I and II, and the subsequent inward rotation of the Phe170$^{2.57}$ and Phe174$^{2.61}$ side chains that occupy the gap pocket[2] (Fig. 3b), the volume of the ligand-binding pocket shrinks from 822 Å^3 in the antagonist-bound structure to 384 Å^3 in the agonist-bound complex, representing a 53% reduction (Fig. 2c,d and Extended Data Table 3).

The agonist-induced conformational changes probably trigger the activation and downstream signalling associated with CB_1. From a more granular perspective, CB_1 seems to use an extended molecular toggle switch that involves a synergistic conformational change between Phe200$^{3.36}$ and Trp356$^{6.48}$, which we refer to as the twin toggle switch (Fig. 4c). In the AM6538-bound structure, Phe200$^{3.36}$ points away from the ligand-binding pocket and forms an aromatic stacking interaction with Trp356$^{6.48}$, which may contribute to stabilization of the receptor in the inactive state (Fig. 4c). In the AM11542-bound structure, the cooperative rotation of helix III and the side-chain flipping of Phe200$^{3.36}$ lead the phenyl ring to point towards the ligand and form hydrophobic interactions with the C1′-gem-dimethyl group of AM11542 (Fig. 4c). Simultaneously, the outwards rotation of helix VI causes the side chain of Trp356$^{6.48}$ to swing away from the ligands (Fig. 4c), disrupting the π–π stacking of the side chains of Phe200$^{3.36}$ and Trp356$^{6.48}$. In comparison to the previously proposed toggle switch of Trp356$^{6.48}$, here we observe the synergistic movement of two residues, Phe200$^{3.36}$ and Trp356$^{6.48}$, during the activation of receptors. We speculate that this twin toggle switch is related to CB_1 activation—a structural observation that is in agreement with a previous modelling study[17,18].

To investigate whether the twin toggle switch concept exists in other receptors, we performed a sequence analysis of class A GPCRs, showing that CB_2, as well as certain chemokine receptors (such as CCR2 and CCR5), possess an aromatic residue at the appropriate position (Phe$^{3.36}$ or Tyr$^{3.36}$) to synergize with the highly conserved tryptophan on helix VI (Trp$^{6.48}$). Furthermore, the highly conserved E/DRY motif and NPXXY motif are also rearranged in the AM11542 agonist-bound CB_1 structure. The polar network around the DRY motif is disrupted during activation (Fig. 4d). Arg214$^{3.50}$ adopts an extended conformation, the intra-helical salt bridge between Asp213$^{3.49}$ and Arg214$^{3.50}$ as

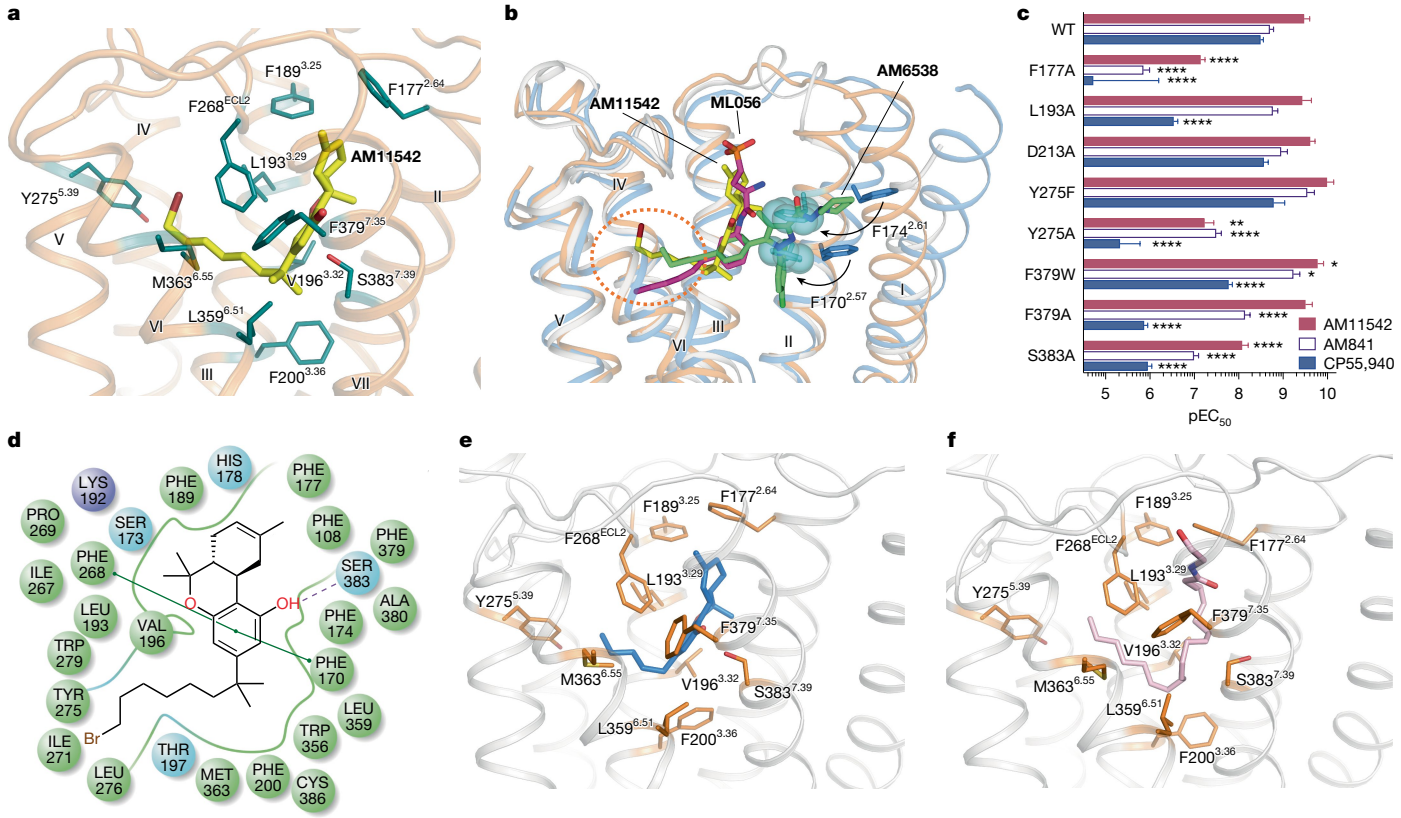

Fig. 3 | AM11542 binding-pocket analysis and molecular docking of Δ⁹-THC and AEA. a, Key residues (deep teal sticks) involved in AM11542 (yellow sticks) binding. **b**, Binding pose comparison of AM11542 (yellow), AM6538 (green) and ML056 (magenta) in their receptors, which are shown in orange, blue and grey, respectively. Phe170$^{2.57}$ and Phe174$^{2.61}$ in AM11542 and AM6538 complexes are shown as blue spheres and sticks, respectively. The orange dotted oval indicates the position of the hydrophobic tails of the three ligands. **c**, Certain substitutions in CB_1 significantly decreased potency in the cAMP assay compared with the agonist response at the wild-type (WT) receptor; this was determined by comparing negative logarithms of the EC_{50} (pEC_{50}) values, and also by an extra-sum-of-squares *F*-test (where each drug is compared with its effect in the wild type, $^*P < 0.05$, $^{**}P < 0.01$, $^{****}P < 0.0001$; data are mean ± s.e.m., $n \geq 3$; Extended Data Table 2). **d**, Summary of AM11542 receptor interactions. Purple ball, positive charged interaction; cyan ball, polar interaction; green ball, hydrophobic interaction; purple dashed line, H-bond; green line, π–π stacking. **e**,**f**, The docking pose of Δ⁹-THC (**e**, blue sticks) and AEA (**f**, pink sticks).

well as the ionic lock between Arg214$^{3.50}$ and Asp338$^{6.30}$ are broken, resulting in rotamer shift of Asp338$^{6.30}$ and movement of helix VI away from helix III (Fig. 4d). Notably, CB_1 shows the largest helix VI bending angle of all known agonist-bound class A GPCRs (without G protein or G protein mimics; Extended Data Fig. 6b). Similarly, the most important rearrangement around the NPXXY region is a partial unwinding of helix VII around Tyr397$^{7.53}$ (Fig. 4d).

A notable feature of the agonist-bound CB_1 structure is the large (53%) reduction in volume in the ligand-binding pocket between agonist- and antagonist-bound structures, and subsequent volume increase in the intracellular G protein-binding site. Such plasticity in the orthosteric binding pocket enables CB_1 to respond to a diverse array of ligands with considerably different sizes, shapes and associated functions, consistent with the ability of CB_1 to modulate such varied physiological and psychological activities.

The ligand-binding volume of all agonist- and antagonist-bound structural pairs in class A GPCRs are compared to investigate whether a similar feature exists in other receptors (Extended Data Table 3). Related to the change in ligand-binding volume, we analysed the helix movement between antagonist- and agonist-bound structures in extracellular and intracellular halves. In most structural pairs, the extracellular half undergoes small changes, whereas larger conformational changes in the intracellular half occur due to movements of helices VI, V and VII (Extended Data Fig. 6a). As an exception to this minimal trigger, CB_1 has the largest ligand-binding pocket volume change, contributed mainly by the movements of the extracellular half of helices I and II. Large inward bending (over 4 Å) of helix VI is also observed in the purinergic receptor $P2Y_{12}$ structure[19,20] (Extended Data Fig. 6a). The balloon-like flexibility of CB_1 in the extracellular region may also occur in other GPCRs. Therefore, multiple, structurally varied receptor models should be considered when designing GPCR agonists and antagonists using structure-based strategies.

Online content

Any methods, additional references, Nature Portfolio reporting summaries, source data, extended data, supplementary information, acknowledgements, peer review information; details of author contributions and competing interests; and statements of data and code availability are available at https://doi.org/10.1038/s41586-025-09454-5.

1. Mechoulam, R., Hanuš, L. O., Pertwee, R. & Howlett, A. C. Early phytocannabinoid chemistry to endocannabinoids and beyond. *Nat. Rev. Neurosci.* **15**, 757–764 (2014).
2. Hua, T. et al. Crystal structure of the human cannabinoid receptor CB1. *Cell* **167**, 750–762 (2016).
3. Ballesteros, J. A. & Weinstein, H. in *Methods in Neurosciences* Vol. 25 (ed. Sealfon S. C.) 366–428 (Academic, 1995).
4. Lemberger, L. Potential therapeutic usefulness of marijuana. *Annu. Rev. Pharmacol. Toxicol.* **20**, 151–172 (1980).
5. Li, H.-L. An archaeological and historical account of cannabis in China. *Econ. Bot.* **28**, 437–448 (1973).
6. Makriyannis, A. 2012 Division of Medicinal Chemistry Award Address. Trekking the cannabinoid road: a personal perspective. *J. Med. Chem.* **57**, 3891–3911 (2014).
7. Shao, Z. et al. High-resolution crystal structure of the human CB1 cannabinoid receptor. *Nature* **540**, 602–606 (2016).

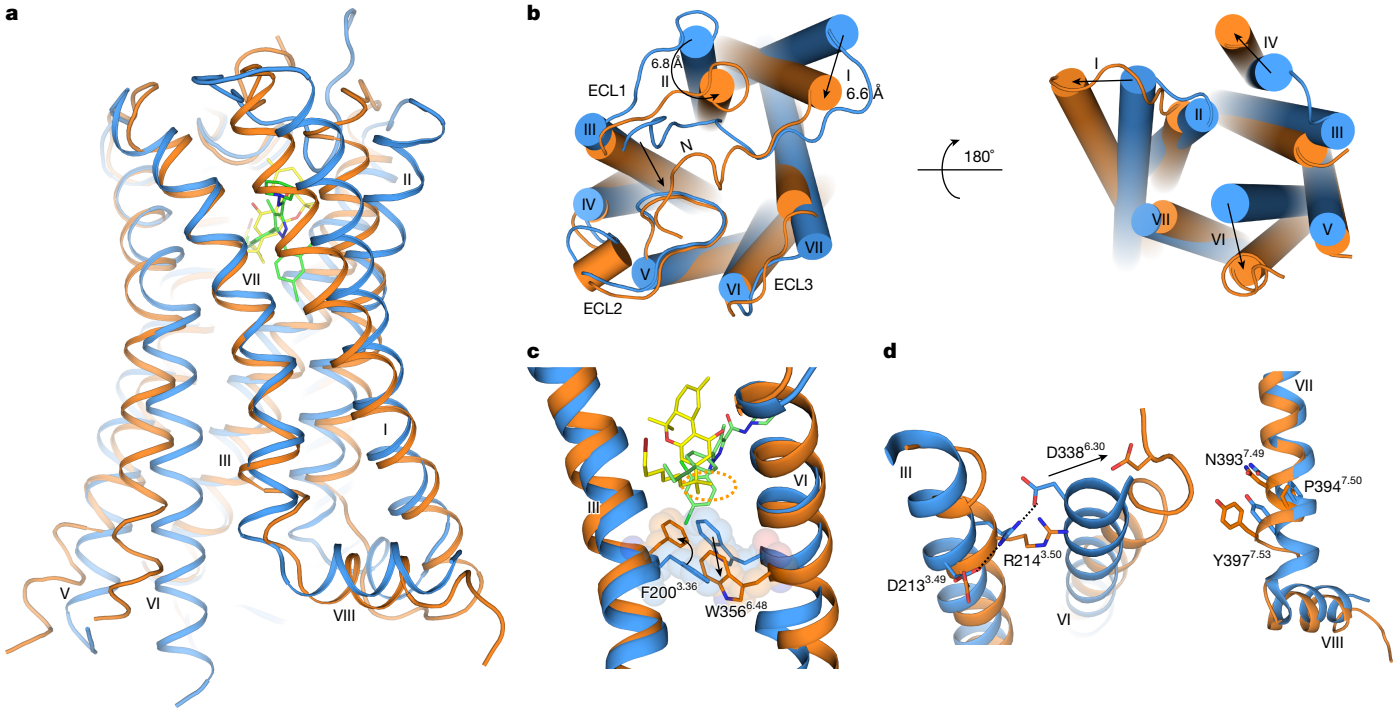

Fig. 4 | Structural comparison of agonist- and antagonist-bound CB_1 complexes. a, Side view of the CB_1–AM11542 complex (where the receptors are in orange and ligands are in yellow) and CB_1–AM6538 complex (receptors in blue and ligands in green). **b**, The extracellular (left) and intracellular (right) views of the compared receptors. N, N terminus. **c**, The twin toggle switch, Phe200$^{3.36}$/Trp356$^{6.48}$, is shown in sticks and spheres. Colour scheme as in **a**. **d**, Rearrangement of DRY (left) and NPXXY (right) motifs in agonist- and antagonist-bound CB_1 structures.

8. Nikas, S. P. et al. The role of halogen substitution in classical cannabinoids: a CB1 pharmacophore model. *AAPS J.* **6**, e30 (2004).
9. Nikas, S. P. et al. Novel 1′,1′-chain substituted hexahydrocannabinols: 9β-hydroxy-3-(1-hexyl-cyclobut-1-yl)-hexahydrocannabinol (AM2389) a highly potent cannabinoid receptor 1 (CB_1) agonist. *J. Med. Chem.* **53**, 6996–7010 (2010).
10. Xie, X. Q., Melvin, L. S. & Makriyannis, A. The conformational properties of the highly selective cannabinoid receptor ligand CP-55,940. *J. Biol. Chem.* **271**, 10640–10647 (1996).
11. Makriyannis, A. & Rapaka, R. S. The medicinal chemistry of cannabinoids: an overview. *NIDA Res. Monogr.* **79**, 204–210 (1987).
12. Ahn, K. H., Bertalovitz, A. C., Mierke, D. F. & Kendall, D. A. Dual role of the second extracellular loop of the cannabinoid receptor 1: ligand binding and receptor localization. *Mol. Pharmacol.* **76**, 833–842 (2009).
13. Feigenbaum, J. J. et al. Nonpsychotropic cannabinoid acts as a functional N-methyl-D-aspartate receptor blocker. *Proc. Natl Acad. Sci. USA* **86**, 9584–9587 (1989).
14. Mechoulam, R. et al. Enantiomeric cannabinoids: stereospecificity of psychotropic activity. *Experientia* **44**, 762–764 (1988).
15. Hanson, M. A. et al. Crystal structure of a lipid G protein-coupled receptor. *Science* **335**, 851–855 (2012).
16. Rasmussen, S. G. et al. Crystal structure of the β_2 adrenergic receptor–Gs protein complex. *Nature* **477**, 549–555 (2011).
17. Singh, R. et al. Activation of the cannabinoid CB1 receptor may involve a W6.48/F3.36 rotamer toggle switch. *J. Pept. Res.* **60**, 357–370 (2002).
18. Tiburu, E. K. et al. Structural biology of human cannabinoid receptor-2 helix 6 in membrane-mimetic environments. *Biochem. Biophys. Res. Commun.* **384**, 243–248 (2009).
19. Zhang, K. et al. Structure of the human $P_{2Y}12$ receptor in complex with an antithrombotic drug. *Nature* **509**, 115–118 (2014).
20. Zhang, J. et al. Agonist-bound structure of the human $P_{2Y}12$ receptor. *Nature* **509**, 119–122 (2014).

Methods

No statistical methods were used to predetermine sample size. However, for mutants in the cAMP accumulation assays, after $n = 3$ was obtained, an additional power analysis was performed ($\alpha = 0.5$; power = 80%) to determine the n required to have confidence in the values produced; further curves were added as indicated.

Synthesis of AM11542 and AM841 (experimental procedures and spectroscopic data)

Experimental procedures for steps a–m (Extended Data Fig. 1) are similar to those we reported previously for closely related systems[9,21,22].

(6a*R*,9*R*,10a*R*)-3-(8-Bromo-2-methyloctan-2-yl)-1-((*tert*-butyldimethylsilyl)oxy)-6,6-dimethyl-6a,7,8,9,10,10a-hexahydro-6*H*-benzo[c]chromene-9-carbaldehyde (12). Colourless oil. ^{1}H NMR (500 MHz, $CDCl_3$) δ 9.63 (d, J = 1.5 Hz, 1H, 9β-CHO), 6.38 (d, J = 2.0 Hz, 1H, Ar–H), 6.32 (d, J = 2.0 Hz, 1H, Ar–H), 3.52–3.46 (t and m as broad d overlapping, t, J = 6.5 Hz, 2H, $-CH_2Br$, m as broad d, J = 13.5 Hz, 1H, C-ring), 2.46–2.33 (m, 2H, C-ring), 2.14–2.06 (m, 1H, C-ring), 2.02–1.96 (m, ^{1}H, C-ring), 1.69 (sextet, J = 6.7 Hz, 2H, 6′-H), 1.52–1.42 (m, 4H, 2′-H, C-ring), 1.42–130 (m and s, overlapping, 5H, $-CH_2-$ of the side chain and 1.39, s, 6-Me), 1.26–1.10 (m, 10H, $-CH_2-$ of the side chain, C-ring and $-C(CH_3)_2-$), 1.09–1.00 (m, s and s, overlapping, 14H as follows: 2H, $-CH_2-$ of the side chain, 1.08, s, 3H, 6-Me, 1.01, s, 9H, $-Si(Me)_2CMe_3$), 0.26 (s, 3H, $Si(Me)_2CMe_3$), 0.15 (s, 3H, $Si(Me)_2CMe_3$). ^{13}C NMR (100 MHz, $CDCl_3$) δ 203.5, 154.5, 154.2, 149.5, 112.5, 109.5, 108.4, 50.5, 49.0, 45.0, 44.4, 37.3, 35.4, 32.6, 30.2, 29.5, 28.8, 28.6, 27.6, 26.9, 26.8, 25.9, 24.5, 18.8, 18.2, −3.6, −4.2. High-resolution mass spectrometry (HRMS) (m/z): $[M + H]^+$ calculated for $C_{31}H_{52}O_3{}^{79}BrSi$, 579.2869 (found, 579.2862); calculated for $C_{31}H_{52}O_3{}^{81}BrSi$, 581.2849 (found, 581.2850).

{(6a*R*,9*R*,10a*R*)-3-(8-Bromo-2-methyloctan-2-yl)-1-[(*tert*-butyldimethylsilyl)oxy]-6,6-dimethyl-6a,7,8,9,10,10a-hexahydro-6H-benzo[c]chromen-9-yl}methanol (13). Colourless viscous oil. ^{1}H NMR (500 MHz, $CDCl_3$) δ 6.37 (d, J = 2.0 Hz, 1H, Ar–H), 6.30 (d, J = 2.0 Hz, 1H, Ar–H), 3.54 (dd, J = 10.5 Hz, J = 5.5 Hz, half of an AB system, 1H, $-CH_2OH$), 3.50–3.43 (dd and t overlapping, especially, 3.48, t, J = 6.5, 7′-H, dd, J = 10.0 Hz, J = 6.5 Hz, half of an AB system, 1H, $-CH_2OH$), 3.18–3.16 (m as broad d, J = 13.0 Hz, 1H, C-ring), 2.40–2.32 (m as td, J = 11.0 Hz, J = 3.0 Hz, 1H, C-ring), 2.04–1.97 (m, 1H, C-ring), 1.94–1.88 (m, 1H, C-ring), 1.8–1.64 (m, 1H, C-ring, 2H, 6′-H), 1.52–1.44 (m, 3H, 2′-H, C-ring), 1.4–1.3 (m and s overlapping, 5H, $-CH_2-$ of the side chain, 6-Me, especially 1.25, s, 3H, 6-Me), 1.24–1.1 (m, s, and s overlapping, 10H, $-C(CH_3)_2-$, $-CH_2-$ of the side chain, C-ring, especially, 1.20, s, 3H, $-C(CH_3)_2-$, and 1.19, s, 3H, $-C(CH_3)_2-$), 1.09–1.02 (s and m overlapping, 5H, 6-Me, $-CH_2-$ of the side chain, especially, 1.06, s, 3H, 6-Me), 1.0 (s, 9H, $Si(Me)_2CMe_3$), 0.82–0.7 (m, 1H, C-ring), 0.23 (s, 3H, $Si(Me)_2CMe_3$), 0.12 (s, 3H, $Si(Me)_2CMe_3$). ^{13}C NMR (100 MHz $CDCl_3$) δ 154.5, 154.3, 149.0, 113.5, 109.7, 108.4, 68.5, 49.6, 45.1, 44.4, 40.5, 37.2, 35.5, 33.2, 32.6, 29.8, 29.5, 28.8, 28.6, 27.6, 27.5, 26.8, 25.9, 24.5, 18,8, 18.2, −3.6, −4.3. HRMS (m/z): $[M + H]^+$ calculated for $C_{31}H_{54}O_3{}^{79}BrSi$, 581.3026 (found, 581.3018); calculated for $C_{31}H_{54}O_3{}^{81}BrSi$, 583.3005 (found, 583.3007).

(6a*R*,9*R*,10a*R*)-3-(8-Bromo-2-methyloctan-2-yl)-9-(hydroxymethyl)-6,6-dimethyl-6a,7,8,9,10,10a-hexahydro-6H-benzo[c]chromen-1-ol (14). tetra-*n*-Butylammonium fluoride (0.72 ml, 0.72 mmol, 1 M solution in anhydrous THF) was added to a solution of **13** (210 mg, 0.36 mmol) in anhydrous THF (9 ml) at −40 °C, under an argon atmosphere. The reaction mixture was stirred for 30 min at the same temperature, and then quenched using a saturated aqueous NH_4Cl solution. Extractive isolation with diethyl ether, and purification by flash column chromatography on silica gel (20–50% ethyl acetate in hexane) gave **14** (164 mg, 96% yield) as a white solid (melting point = 68–70 °C). ^{1}H NMR (500 MHz, $CDCl_3$) δ 6.35 (d, J = 1.0 Hz, 1H, Ar–H), 6.18 (d, J = 1.5 Hz, 1H, Ar–H), 4.75 (broad s, 1H, ArOH), 3.61–3.42 (m and t overlapping, 4H, $-CH_2OH$, 7′-H, especially, 3.49, t, J = 6.5 Hz, 2H, $-CH_2OH$), 3.23–3.16 (m as broad d, J = 13.0 Hz, 1H, C-ring), 2.52–2.44 (m as td, J = 11.0 Hz, J = 2.5 Hz, 1H, C-ring), 2.02–1.91 (m, 2H, C-ring), 1.82–1.74 (m, 1H, C-ring), 1.72–1.64 (m, 1H, 6′-H), 1.54–1.46 (m, 3H, 2′-H, C-ring), 1.44–1.31 (s and m overlapping, 5H, 6-Me, $-CH_2-$ of the side chain, especially, 1.39, s, 3H, 6-Me), 1.29–1.15 (s, and m overlapping, 10H, $-C(CH_3)_2-$, $-CH_2-$ of the side chain, C-ring, especially, 1.20, s, 6H, $-C(CH_3)_2-$), 1.10–1.01 (s and m overlapping, 5H, 6-Me, $-CH_2-$ of the side chain, especially, 1.09, s, 3H, 6-Me), 0.89–0.78 (m as q, J = 11.5 Hz, 1H, C-ring). ^{13}C NMR (100 MHz $CDCl_3$) δ 154.7, 154.4, 149.7, 109.6, 107.9, 105.4, 68.5, 49.3, 45.2, 44.2, 40.5, 37.2, 34.9, 33.1, 32.6, 29.7, 29.5, 28.7, 28.6, 27.7, 27.4, 26.7, 24.4, 19.0. HRMS (m/z): $[M + H]^+$ calculated for $C_{25}H_{40}O_3{}^{79}Br$, 467.2161 (found, 467.2162); calculated for $C_{25}H_{40}O_3{}^{81}Br$, 469.2140 (found, 469.2144).

(6a*R*,9*R*,10a*R*)-3-(8-Azido-2-methyloctan-2-yl)-9-(hydroxymethyl)-6,6-dimethyl-6a,7,8,9,10,10a-hexahydro-6H-benzo[c]chromen-1-ol (15). *N*,*N*,*N*′,*N*′-tetramethylguanidinium azide (1.6 g, 10.2 mmol) was added to a stirred solution of **14** (160 mg, 0.34 mmol) in anhydrous CH_3Cl/CH_3NO_2 (1:1 mixture, 6 ml) at room temperature under an argon atmosphere, and stirring was maintained for one day. On completion, the reaction was quenched with water and diluted with CH_2Cl_2. The organic phase was washed with brine, dried over $MgSO_4$ and concentrated in vacuo. Purification by flash column chromatography on silica gel (50–80% diethyl ether in hexanes) gave 124 mg of **15** as a white solid in 84% yield (melting point = 59–61 °C). Infrared (neat): 3,343 (broad, OH), 2,931, 2,860, 2,093 (s, N_3), 1,713, 1,621, 1,537, 1,413, 1,331, 1,268, 1,138, 1,011, 967, 839 cm^{-1}. ^{1}H NMR (500 MHz, $CDCl_3$): δ 6.35 (d, J = 1.0 Hz, 1H, Ar–H), 6.19 (d, J = 1.5 Hz, 1H, Ar–H), 4.81 (br s, 1H, ArOH), 3.57–3.47 (m, 2H, $-CH_2OH$), 3.23–3.17 (m and t overlapping 3H, C-ring, 7′-H, especially, 3.21, t, J = 6.5 Hz, 2H, 7′-H), 2.52–2.44 (m as td, J = 11.0 Hz, J = 2.5 Hz, 1H, C-ring), 2.02–1.91 (m, 2H, C-ring), 1.82–1.74 (m, 1H, C-ring), 1.56–1.46 (m 5H, 6′-H, 2′-H, C-ring), 1.38 (s, 3H, 6-Me), 1.35–1.26 (m, 2H, $-CH_2-$ of the side chain), 1.25–1.11 (s and m overlapping, 10H, $-C(CH_3)_2-$, $-CH_2-$ of the side chain, C-ring, especially, 1.20, s, 6H, $-C(CH_3)_2-$), 1.10–1.02 (s and m overlapping, 5H, 6-Me, $-CH_2-$ of the side chain, especially, 1.09, s, 3H, 6-Me), 0.87–0.78 (m as q, J = 12 Hz, ^{1}H, C-ring). ^{13}C NMR (100 MHz $CDCl_3$) δ 154.6, 154.5, 149.7, 109.6, 107.8, 105.4, 68.5, 51.5, 49.3, 44.2, 40.5, 37.2, 34.9, 33.1, 29.7, 29.6, 28.8, 28.7, 27.7, 27.4, 26.5, 24.4, 19.0. HRMS (m/z): $[M]^+$ calculated for $C_{25}H_{40}N_3O_3$, 430.3070 (found, 430.3065).

(6a*R*,9*R*,10a*R*)-9-(Hydroxymethyl)-3-(8-isothiocyanato-2-methyloctan-2-yl)-6,6-dimethyl-6a,7,8,9,10,10a-hexahydro-6H-benzo[c]chromen-1-ol (AM841). Triphenyl phosphine (365 mg, 1.4 mmol) was added to a solution of **15** (120 mg, 0.28 mmol) in anhydrous THF (5.6 ml) at room temperature. Carbon disulfide (0.55 ml, 8.4 mmol) was then added dropwise and the reaction mixture was stirred for an additional 10 h at the same temperature. Following completion, the reaction mixture was concentrated under reduced pressure and purified by flash column chromatography on silica gel (50–80% diethyl ether in hexanes) to give 95 mg of AM841 as a white solid in 76% yield (melting point = 63–65 °C). IR (neat): 3,332 (broad, OH), 2,931, 2,860, 2,093 (s, NCS), 1,620, 1,537, 1,451, 1,413, 1,331, 1,269, 1,137, 1,037, 966, 838 cm^{-1}. ^{1}H NMR (500 MHz, $CDCl_3$): δ 6.35 (d, J = 1.5 Hz, 1H, Ar–H), 6.19 (d, J = 2.0 Hz, 1H, Ar–H), 4.76 (broad s, 1H, ArOH), 3.52 (m, 2H, $-CH_2OH$), 3.46 (t, J = 6.5 Hz, 2H, 7′-H), 3.22–3.16 (m as d, J = 13 Hz, 1H, C-ring), 2.51–2.44 (m as td, J = 11.0 Hz, J = 2.5 Hz, 1H, C-ring), 2.02–1.91 (m, 2H, C-ring), 1.82–1.74 (m, 1H, C-ring), 1.65–1.56 (m, 2H, 6′-H), 1.54–1.46 (m, 3H, 2′-H, C-ring), 1.39 (s, 3H, 6-Me), 1.37–1.29 (m, 2H, $-CH_2-$ of the side chain group), 1.26–1.11 (s and m overlapping, 10H, $-C(CH_3)_2-$, $-CH_2-$ of the side chain, C-ring, especially, 1.20, s, 6H, $-C(CH_3)_2-$), 1.10–1.03 (s and m overlapping, 5H, 6-Me, $-CH_2-$ of the side chain, especially, 1.09, s, 3H, 6-Me), 0.87–0.7 (m as q, J = 12 Hz, 1H, C-ring). ^{13}C NMR (100 MHz $CDCl_3$) δ 154.6 (ArC-1 or ArC-5), 154.5 (ArC-5 or ArC-1), 130.1

(NCS), 149.6 (tertiary aromatic), 109.7 (tertiary aromatic), 107.8 (ArC-2 or ArC-4), 105.3 (ArC-4 or ArC-2), 68.5 (−CH_2OH), 49.3, 45.0, 44.1, 40.5, 37.2, 35.0, 33.1, 29.8, 29.7, 29.3, 28.7, 28.6, 27.7, 27.4, 26.3, 24.3, 19.0. HRMS (*m/z*): $[M]^+$ calculated for $C_{26}H_{40}NO_3S$, 446.2729 (found, 446.2726).

(−)−7′-Bromo-1′,1′-dimethylheptyl-Δ^8-tetrahydrocannabinol (AM11542)

Experimental procedures for the synthesis and purification, along with spectroscopic and analytical data were reported in a previous work from our laboratory[8].

Purification of CB_1–flavodoxin protein and crystallization in lipidic cubic phase

CB_1–flavodoxin construction, expression and membrane preparation were performed using the same procedure as described previously[2]. In brief, the construct has truncations of residues 1–98, 307–331 and 415–472, the flavodoxin (Protein Data Bank (PDB) accession 1I1O, molecular mass 14.9 kDa, with Tyr98Trp substitution) fusion protein was fused to the truncated third intracellular loop of the human *CNR1* (also known as *CB1*) gene. The resulting CB_1–flavodoxin chimera sequence was subcloned into a modified mammalian expression vector pTT5 that contains a haemagglutinin signal sequence, a Flag tag and 10× His tag, followed by a tobacco etch virus (TEV) protease cleavage site, before the N terminus of the chimera sequence. The *CNR1* gene was further modified by introducing four rationally designed mutations[23], Thr210$^{3.46}$Ala, Glu273$^{5.37}$Lys, Thr283$^{5.47}$Val and Arg340$^{6.32}$Glu, using standard QuickChange PCR. The protein was expressed using the FreeStyle 293 Expression system (Invitrogen) in HEK293F cells for 48 h, and the membrane was washed repeatedly using hypotonic buffer with low and high salt. Notably, the receptor used for crystallization was capable of binding to [^{3}H]CP55,940 and this binding could be replaced by AM11542 (K_i = 0.29 (0.17–0.50) nM), AM841 (K_i = 0.53 (0.36–0.80) nM) as the wild-type receptor, and cold CP55,940 (K_i = 2.0 (1.2–3.5) nM). This CB_1 construct yielded no signalling in signalling assays (not shown), which is probably due to the flavodoxin insert that prevents coupling secondary effectors; however, the individual point mutations did not interfere with agonist activity except for Thr210$^{3.46}$Ala, which has been previously reported[23]. These controls are summarized in Extended Data Fig. 4c and Extended Data Table 2.

Purified membranes were thawed at room temperature and then incubated with the corresponding ligand (AM11542 or AM841; 20 μM) in the presence of 1.0 mg ml^{-1} iodoacetamide, and EDTA-free protease inhibitor cocktail (Roche) for 30 min at room temperature, and then further incubated at 4 °C for 3 h. The membranes were then solubilized with 50 mM HEPES (pH 7.5), 500 mM NaCl, 1% (w/v) lauryl maltose neopentyl glycol (LMNG, Anatrace) and 0.2% (w/v) cholesterol hemisuccinate (CHS, Sigma-Aldrich) at 4 °C for 2.5–3.0 h. The supernatants containing the solubilized CB_1 proteins were isolated by high-speed centrifugation, and then incubated with TALON IMAC resin (Clontech) and 20 mM imidazole, at 4 °C overnight. The resin was washed with 15 column volumes of washing buffer I containing 25 mM HEPES (pH 7.5), 500 mM NaCl, 10% (v/v) glycerol, 0.1% (w/v) LMNG, 0.02% (w/v) CHS, 30 mM imidazole and 20 μM AM11542 or AM841, and five column volumes of washing buffer II containing 25 mM HEPES (pH 7.5), 500 mM NaCl, 10% (v/v) glycerol, 0.03% (w/v) LMNG, 0.015% (w/v) CHS, 50 mM imidazole and 20 μM AM11542 or AM841. The proteins were eluted by 2.5 column volumes of eluting buffer containing 25 mM HEPES (pH 7.5), 500 mM NaCl, 10% (v/v) glycerol, 0.01% (w/v) LMNG, 0.002% (w/v) CHS, 250 mM imidazole and 20 μM AM11542 or AM841. PD MiniTrap G-25 column (GE Healthcare) was used to remove imidazole. The protein was then treated overnight with TEV protease to cleave the N-terminal Flag/His tags from the proteins. Finally, the purified CB_1 protein together with TEV protease was concentrated to about 35 mg ml^{-1} with a 100 kDa cutoff concentrator (Sartorius) and used in crystallization trials. The protein yield and monodispersity were tested by analytical size exclusion chromatography.

Protein samples were reconstituted into a lipidic cubic phase (LCP) by mixing them with molten lipid (90% (w/v) monoolein and 10% (w/v) cholesterol) at a protein:lipid ratio of 2:3 (v/v) using a mechanical syringe mixer[24]. The LCP crystallization trials were performed using an NT8-LCP crystallization robot (Formulatrix). Then, 96-well glass sandwich plates were incubated and imaged at 20 °C using an automatic incubator/imager (RockImager 1000, Formulatrix). For the CB_1–AM11542 complex, the crystals grew in conditions of 0.1 M sodium cacodylate trihydrate pH 6.4, 300–350 mM $C_4H_4KNaO_6$, 30% PEG400 and grew to the full size in one week. For the CB_1–AM841 complex, the crystals appeared after two days in 0.1 M sodium cacodylate trihydrate pH 6.2, 120 mM $C_6H_5Na_3O_7{\cdot}2H_2O$, 30% PEG400 and 100 mM glycine and reached their full size after one week. The crystals were collected using micromounts (MiTeGen) and flash-frozen in liquid nitrogen.

Data collection, structure solution and refinement

X-ray diffraction data were collected at GM/CA-CAT beamline 23ID-B at the Advanced Photon Source, Argonne National Laboratory, using an Eiger 16 M detector (X-ray wavelength 1.0000 Å) and at beamline X06SA of the Swiss Light Source. The crystals were exposed with a 10 μm minibeam for 0.2 s and 0.2° oscillation per frame, a rastering system was applied to find the best diffracting parts of single crystals[25,26]. The XDS program package[27] was used for integrating and scaling data from the 16 crystals for the CB_1–AM11542 complex and 10 crystals for the CB_1–AM841 complex. Initial phase information was obtained by molecular replacement with Phaser[28] using the receptor portion of CB_1 (PDB code 5TGZ) and flavodoxin structure (PDB code 1I1O) as search models. Refinement was performed with Phenix[29] and Buster[30] followed by manual examination and rebuilding of the refined coordinates in the program COOT[31] using both $|2F_o| - |F_c|$ and $|F_o| - |F_c|$ maps.

Radioligand binding assay

Radioligand binding to determine agonist affinity and wash resistant residency was determined as previously described[2] using [^{3}H]CP55,940 (specific activity: 81.1 Ci mmol^{-1}, NDSP, NIDA) and an excess of CP55,940 to determine non-specific binding. For washout experiments at the wild-type CB_1, specifically, membranes were incubated at 37 °C for 1 h in the presence of vehicle (buffer with 1% DMSO), 1 nM AM11542, 10 nM AM841 or 4 nM CP55,940 followed by resuspension in assay buffer containing 1% BSA and incubated at 37 °C for 30 min (to remove non-specifically bound ligands); this was repeated twice to wash away bound ligands before the saturation radioligand binding assay on membranes (37 °C for 1–4 h as indicated). K_i and B_{max} were calculated through nonlinear regression analysis using GraphPad Prism 7.0 (n = 3–6).

Wild-type and mutant CB_1–CHO cell line generation for functional studies

Cell line generation and maintenance was conducted as described previously[2] and briefly described here. The N-terminally 3×HA-tagged CB_1 cDNA was obtained the cDNA Resource Center (http://cdna.org) and subcloned into a mouse stem-cell virus for cell line transduction (pMSCV-puro, Clontech). Point mutations were introduced to the N-terminally 3 × HA-tagged CB_1 cDNA in MSCV retroviral vector by using the Site-Directed Mutagenesis kit (New England Biolabs) (Phe177Ala, Leu193Ala, Asp213Ala, Tyr275Ala, Tyr275Phe, Phe379Ala, Phe379Trp, Ser383Ala). Generation of Phe379 mutants was described previously[2]. Wild-type and mutant CB_1 constructs were packaged into a retrovirus using the Phoenix package system (Allele Biotechnology, ABP-RVC-10001), and the produced retroviruses were applied to CHO-K1 (ATCC, CCL-61) cells for gene transduction. Cells were maintained in DMEM/F-12 medium supplemented with 10% FBS, 1% penicillin–streptomycin, and 5 mg ml^{-1} puromycin (Invitrogen) for stable line selection at 37 °C (5% CO_2 and 95% relative humidity). Cell lines were

negative for mycoplasma. Refer to Extended Data Fig. 4a for details on the primers used to make mutant CB_1 receptors.

Quantitative flow cytometry

Validation of cell-surface expression of the HA-tagged wild-type and mutant CB_1 receptors expressed in CHO-K1 cells was obtained by anti-HA antibody staining followed by quantitative flow cytometry and visually confirmed by confocal imaging. In brief, cells were serum-starved for 30 min at 37 °C, collected in 5 mM EDTA and fixed with 4% paraformaldehyde for 10 min at 4 °C. Cells were washed twice with PBS and resuspended in PBS containing 1% FBS and 5 mM EDTA. Cells were incubated with anti-HA AlexaFluor488-conjugated antibody (1:1,000) for 30 min at 4 °C, washed twice with PBS and again resuspended in PBS containing 1% FBS and 5 mM EDTA. Fluorescence was recorded using a BD Canto flow cytometer (excitation/emission: 488/525 nm). Approximately 50,000 events were recorded for each cell line. Single cell clones were selected based on positive surface expression used to proliferate the mutant cell lines. Refer to Extended Data Fig. 4a for details on the primers used to make mutant CB_1 receptors.

cAMP accumulation assay

Inhibition of forskolin-stimulated cAMP was determined using the CISBIO cAMP homogeneous time-resolved fluorescence resonance energy transfer (Cisbio Assays) as previously described[2].

Docking and molecular dynamics simulations

Prediction of ligand binding to CB_1 was performed using Schrödinger Suite 2015-4. Processing of the protein structure was performed using the Protein Preparation Wizard. Ligands were converted from 2D to 3D structures using LigPrep. Rigid protein docking in extra precision was used with Glide v.6.9 (refs. 32–34) (induced fit docking protocol 2015-4, Glide v.6.4, Primer v.3.7, Schrödinger, ref. 35) for molecular docking of Δ^9-THC and AEA.

Molecular dynamics simulations were performed using GROMACS v.5.1.2 (ref. 36), alongside Amber 14 (http://ambermd.org/). CB_1 in complex with each agonist in the pocket (binding modes predicted by molecular docking) was embedded into a pre-equilibrated 1-palmytoil-2-oleoyl-*sn*-glycerol-3-phosphatidylcholine (POPC) lipid bilayer using the membed tool in GROMACS program. The topology files of ligands and POPC molecules were generated using the AmberTools function in the UCSF Chimera program[37] v.1.10.2 and converted to the GROMACS format with the ACPYPE tool[38]. The systems were solvated with water; sodium ions were added to 0.15 M in water, and chloride ions were added to neutralize the system. Molecular dynamics simulations were performed in the NPT ensemble at a temperature of 310 K and pressure of 1 atm, using semi-isotropic coupling. First, each system was balanced position-restrained molecular dynamics for 15 ns (the total energy was stable). Then 1-µs molecular dynamics simulations with no position restraints were performed on each system for two independent runs, and these trajectories are used for analysis. Ligand r.m.s.d. value was calculated with protein C_α atoms superimposed to the starting structure.

Comparison of agonist- and antagonist-bound class A GPCR structures

Seventeen crystal structures of seven GPCRs that have both agonist- and antagonist-bound structures were selected from the PDB[39]. Among them, there are 24, 32 and 21 structures for the β_2-adrenergic receptor, rhodopsin and A_{2A} adenosine receptor, respectively. To pick representative structures of the three GPCRs, their PDB structures were clustered using the R package Bio3D[40] on the basis of differences in r.m.s.d. The following structures from each cluster were manually picked. Agonist and arrestin-bound structures include CB_1 (this study; PDB code 5XRA), β_2-adrenergic receptor (PDB codes 3SN6 and 4LDL), µ-opioid receptor (PDB code 5C1M), M_2 muscarinic receptor (PDB code 4MQS), rhodopsin (PDB codes 2X72 and 4ZWJ (arrestin-bound)), A_{2A} adenosine receptor (PDB codes 3QAK, 5G53) and P_{2Y} purinoceptor 12 (PDB code 4PXZ). Antagonist-bound structures include CB_1 (PDB code 5TGZ), β_2-adrenergic receptor (PDB code 3NY8), µ-opioid receptor (PDB code 4DKL), M_2 muscarinic receptor (PDB code 3UON), rhodopsin (PDB code 1U19), A_{2A} adenosine receptor (PDB code 4EIY) and P_{2Y} purinoceptor 12 (PDB code 4NTJ).

Binding pocket volume calculation

These structures were processed by the Protein Preparation Wizard in Schrödinger Suite 2015-4. The volume of binding pockets was calculated by using Sitemap.

The r.m.s.d. values of extracellular and intracellular transmembrane helices

Seven conserved residues close to the middle of each helix with Ballesteros–Weinstein numbering 1.50, 2.50, 3.39, 4.50, 5.50, 6.50 and 7.49 were used to divide the seven transmembrane helices into extracellular and intracellular parts. The whole structures of each pair of agonist/antagonist-bound structures were aligned in UCSF Chimera[37]; the r.m.s.d. values of C_α atoms in the extracellular and intracellular parts were then calculated using UCSF Chimera.

Quantification and statistical analysis

Concentration–response curves, expressed as fold over basal, were fit to a nonlinear regression (three-parameter) model in Prism (v.7.0, GraphPad Software). For functional analysis of wild-type and CB_1 mutants, pEC_{50} and E_{max} values were calculated from nonlinear regression (three parameter) analysis of mean data from independent experiments performed in duplicate. In Fig. 1d, CP55,940 served as an assay control and was assayed in parallel with all compounds ($n = 24$ for CP55,940, $n = 17$ for AM11542, $n = 32$ for AM841 and $n = 6$ for THC). In Extended Data Table 2, the number of independent experiments (n) is indicated in the table. Statistical analyses comparing pEC_{50} between CB_1 wild-type and mutant lines were conducted using an extra-sum-of-squares F-test in Prism software v.9.0.

Reporting summary

Further information on research design is available in the Nature Portfolio Reporting Summary linked to this article.

Data availability

Atomic coordinates and structures have been deposited in the PDB with accession codes 5XRA (CB_1–AM11542) and 5XR8 (CB_1–AM841). Source Data are provided with this paper.

21. Nikas, S. P. et al. A concise methodology for the synthesis of (–)-Δ9-tetrahydrocannabinol and (–)-Δ9-tetrahydrocannabivarin metabolites and their regiospecifically deuterated analogs. *Tetrahedron* **63**, 8112–8113 (2007).
22. Kulkarni, S. et al. Novel C-ring-hydroxy-substituted controlled deactivation cannabinergic analogues. *J. Med. Chem.* **59**, 6903–6919 (2016).
23. D'Antona, A. M., Ahn, K. H. & Kendall, D. A. Mutations of CB1 T210 produce active and inactive receptor forms: correlations with ligand affinity, receptor stability, and cellular localization. *Biochemistry* **45**, 5606–5617 (2006).
24. Caffrey, M. & Cherezov, V. Crystallizing membrane proteins using lipidic mesophases. *Nat. Protocols* **4**, 706–731 (2009).
25. Cherezov, V. et al. Rastering strategy for screening and centring of microcrystal samples of human membrane proteins with a sub-10 µm size X-ray synchrotron beam. *J. R. Soc. Interface* **6**, S587–S597 (2009).
26. Chun, E. et al. Fusion partner toolchest for the stabilization and crystallization of G protein-coupled receptors. *Structure* **20**, 967–976 (2012).
27. Kabsch, W. XDS. *Acta Crystallogr. D* **66**, 125–132 (2010).
28. McCoy, A. J. et al. Phaser crystallographic software. *J. Appl. Crystallogr.* **40**, 658–674 (2007).
29. Adams, P. D. et al. PHENIX: a comprehensive Python-based system for macromolecular structure solution. *Acta Crystallogr. D* **66**, 213–221 (2010).
30. Smart, O. S. et al. Exploiting structure similarity in refinement: automated NCS and target-structure restraints in BUSTER. *Acta Crystallogr. D* **68**, 368–380 (2012).
31. Emsley, P., Lohkamp, B., Scott, W. G. & Cowtan, K. Features and development of Coot. *Acta Crystallogr. D* **66**, 486–501 (2010).

32. Friesner, R. A. et al. Glide: a new approach for rapid, accurate docking and scoring. 1. Method and assessment of docking accuracy. *J. Med. Chem.* **47**, 1739–1749 (2004).
33. Friesner, R. A. et al. Extra precision glide: docking and scoring incorporating a model of hydrophobic enclosure for protein–ligand complexes. *J. Med. Chem.* **49**, 6177–6196 (2006).
34. Halgren, T. A. et al. Glide: a new approach for rapid, accurate docking and scoring. 2. Enrichment factors in database screening. *J. Med. Chem.* **47**, 1750–1759 (2004).
35. Xu, T. et al. Induced-fit docking enables accurate free energy perturbation calculations in homology models. *J. Chem. Theory Comput.* **18**, 5710–5724 (2022).
36. Abraham, M. J. et al. GROMACS: high performance molecular simulations through multi-level parallelism from laptops to supercomputers. *SoftwareX* **1–2**, 19–25 (2015).
37. Pettersen, E. F. et al. UCSF Chimera—a visualization system for exploratory research and analysis. *J. Comput. Chem.* **25**, 1605–1612 (2004).
38. Sousa da Silva, A. W. & Vranken, W. F. ACPYPE—AnteChamber PYthon Parser interfacE. *BMC Res. Notes* **5**, 367 (2012).
39. Berman, H. M. et al. The Protein Data Bank. *Nucl. Acids Res.* **28**, 235–242 (2000).
40. Skjærven, L., Yao, X. Q., Scarabelli, G. & Grant, B. J. Integrating protein structural dynamics and evolutionary analysis with Bio3D. *BMC Bioinf.* **15**, 399 (2014).

Acknowledgements This work was supported by the NSF of China (grant no. 31330019 to Z.-J.L.), the MOST of China (grant nos. 2014CB910400 and 2015CB910104 to Z.-J.L.), NSF of Shanghai (grant no. 16ZR1448500 to S.Z.), the Key R&D Program of China (grant no. 2016YCF0905902 to S.Z.), the NIH (grant nos. R01DA041435 to R.C.S. and A.M., P01DA009158 to A.M. and L.M.B., and R37DA023142 to A.M.), NSF grants, the Shanghai Municipal Government, ShanghaiTech University and the GPCR Consortium. The diffraction data were collected at GM/CA@APS of Argonne National Laboratory, X06SA@SLS of the Paul Scherrer Institute, and BL41XU@Spring-8 with JASRI proposals 2015B1031 and 2016A2731. We thank M. Wang, C.-Y. Huang, V. Olieric, M. Audet and M.-Y. Lee for their help with data collection, A. Walker for critical review of the manuscript and F. Sun for high-resolution mass spectrometry analysis. We thank E. Stahl, C. Brust and V. Dang from UF Scripps for their contributions to making cell lines, mutations and generating the functional data.

Author contributions T.H. performed crystallization, data collection, structure determination and analysis. K.V., S.P.N. and S.J. designed, synthesized and characterized the ligands. Y.W. performed the docking and molecular dynamics simulations. L.Q. and M.P. collected and processed data, and refined the structures. G.W.H. and M.A.H. contributed to structure refinement and data analysis. J.-H.H. conducted the functional studies and worked on mutations. A.K. performed the radioligand binding assays. K.D. performed structure analysis. X.L. and H.L. performed the molecular dynamics simulations. S.Z. supervised the structure and simulation analyses. L.M.B. designed and supervised the functional and kinetic studies. A.M. supervised the conceptual design, synthesis and characterization of the agonist. R.C.S. conceived the project, and supervised the data analysis. Z.-J.L. designed and supervised the experiments, and analysed the data. Z.-J.L., T.H., R.C.S., A.M., L.M.B. and S.Z. wrote the manuscript with discussions and improvements from M.A.H., K.V., S.P.N. and Y.W.

Competing interests A.M. is a founder of MAKScientific. R.C.S. is the chief executive and a board member of Structure Therapeutics. The other authors declare no competing interests.

Additional information

Supplementary information The online version contains supplementary material available at https://doi.org/10.1038/s41586-025-09454-5.

Correspondence and requests for materials should be addressed to Suwen Zhao, Laura M. Bohn, Alexandros Makriyannis or Zhi-Jie Liu.

Peer review information *Nature* thanks the anonymous reviewers for their contribution to the peer review of this work.

Synthesis of AM841

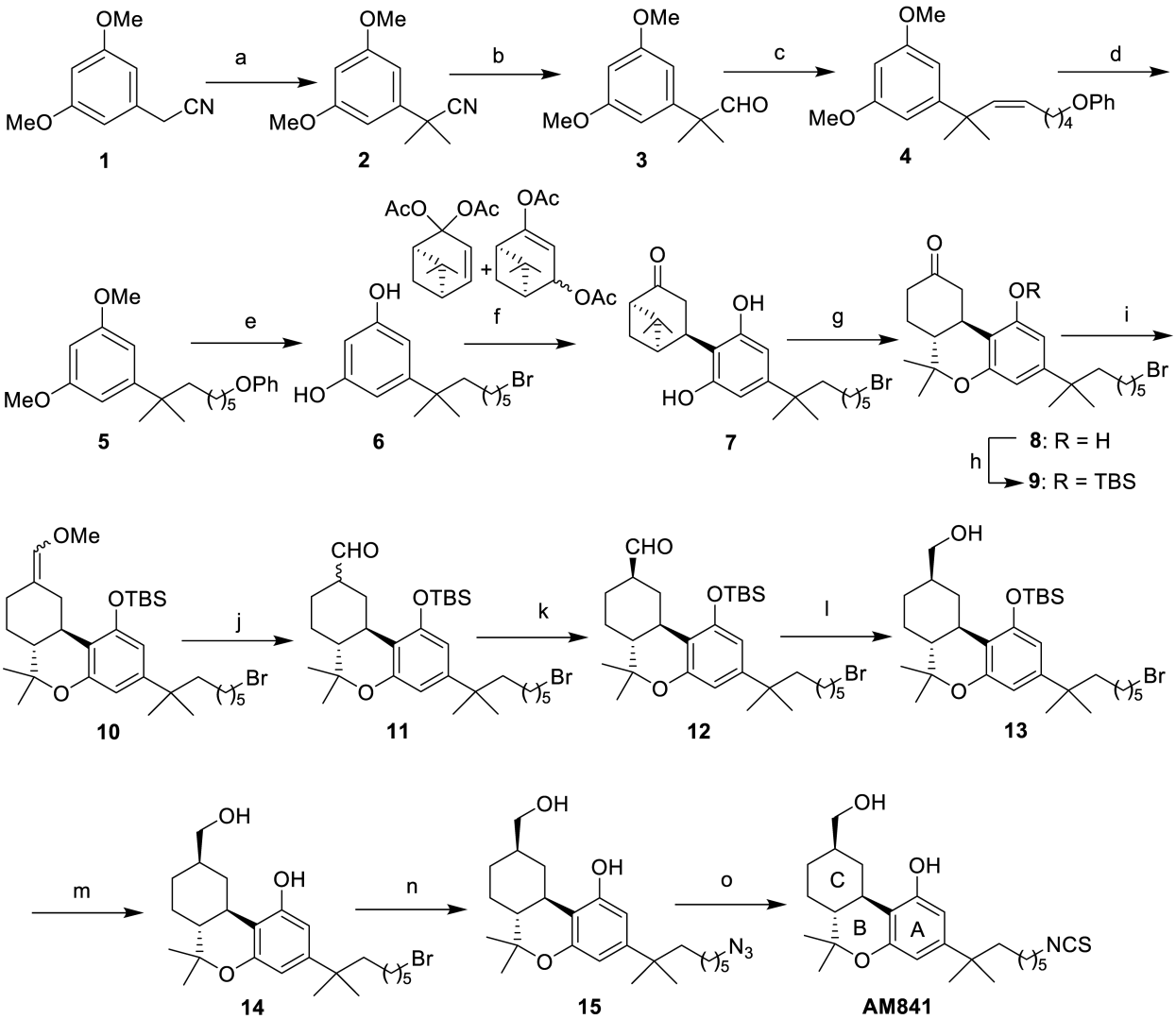

Synthesis of AM11542

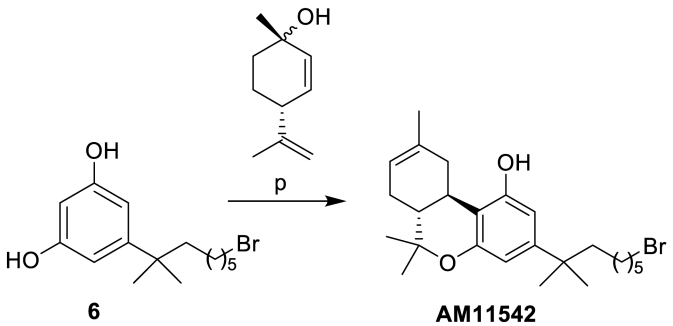

Extended Data Fig. 1 | Synthesis of AM841 and AM11542. Reagents and conditions: (a) CH_3I, NaH, DMF, 0 °C to room temperature, 2 h, 95%; (b) DIBAL-H, CH_2Cl_2, −78 °C, 0.5 h, 87%; (c) $Br^-P^+Ph_3(CH_2)_5OPh$, $(Me_3Si)_2NK$, THF, 0–10 °C, 30 min, then addition to **3**, 0 °C to room temperature, 2 h, 96%; (d) H_2, 10% Pd/C, AcOEt, room temperature, 2.5 h, 89%; (e) BBr_3, CH_2Cl_2, −78 °C to room temperature, 6 h, 85%; (f) diacetates, *p*-TSA, $CHCl_3$, 0 °C to room temperature, 4 days, 64%; (g) TMSOTf, $CH_2Cl_2/MeNO_2$, 0 °C to room temperature, 3 h, 71%; (h) TBDMSCl, imidazole, DMAP, DMF, room temperature, 12 h, 85%; (i) $Cl^-Ph_3P^+CH_2OMe$, $(Me_3Si)_2NK$, THF, 0 °C to room temperature, 1 h, then addition to **9**, 0 °C to room temperature, 1.5 h, 73%; (j) Cl_3CCOOH, CH_2Cl_2, room temperature, 50 min, 95%; (k) K_2CO_3, EtOH, room temperature, 3 h, 84%; (l) $NaBH_4$, EtOH, 0 °C, 30 min, 98%; (m) TBAF, THF, −40 °C, 30 min, 96%; (n) TMG-N_3, $CHCl_3/MeNO_2$, room temperature, 18 h, 84%; (o) PPh_3, CS_2, THF, room temperature, 10 h, 76%; (p) (+)-*cis/trans-p*-mentha-2,8-dien-1-ol, *p*-TSA, benzene, reflux 4 h, 65%.

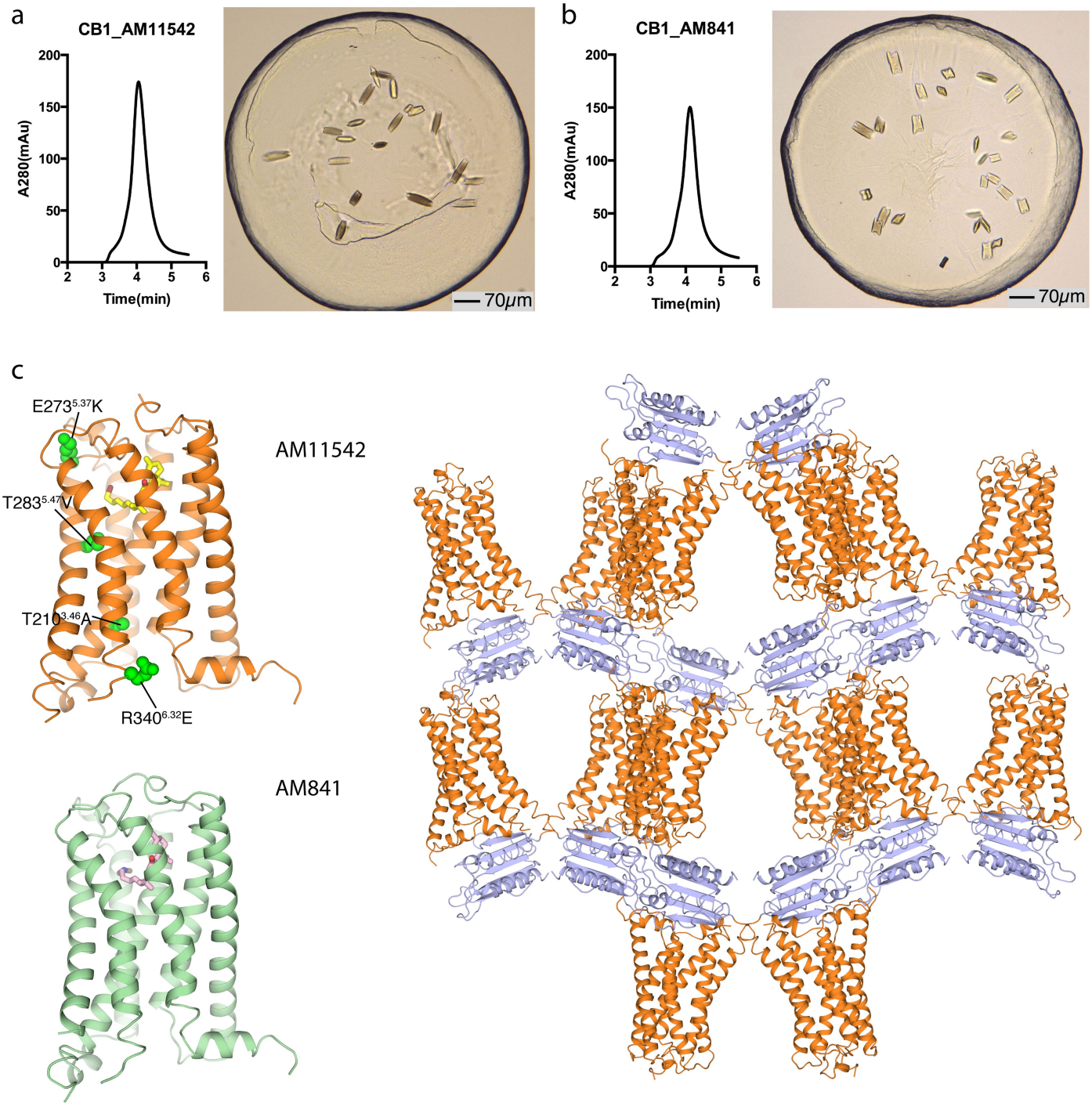

Extended Data Fig. 2 | Analytical size exclusion chromatography profile and crystals of CB_1–AM11542/AM841 complex. a, Analytical size exclusion chromatography and crystal image of the CB_1–AM11542 complex. Scale bar, 70 μm. **b**, Analytical size exclusion chromatography and crystal image of the CB_1–AM841 complex. Scale bar, 70 μm. **c**, The overall structures of CB_1–AM11542 and CB_1–AM841 complexes and crystal packing of CB_1–AM11542; receptor is in orange (AM11542)/green (AM841) colour and the flavodoxin fusion protein is in purple-blue colour. The agonists AM11542 (yellow) and AM841 (pink) are shown in sticks representation. The four single mutations $T210^{3.46}A$, $E273^{5.37}K$, $T283^{5.47}V$ and $R340^{6.32}E$ are shown as green spheres in the CB_1–AM11542 structure.

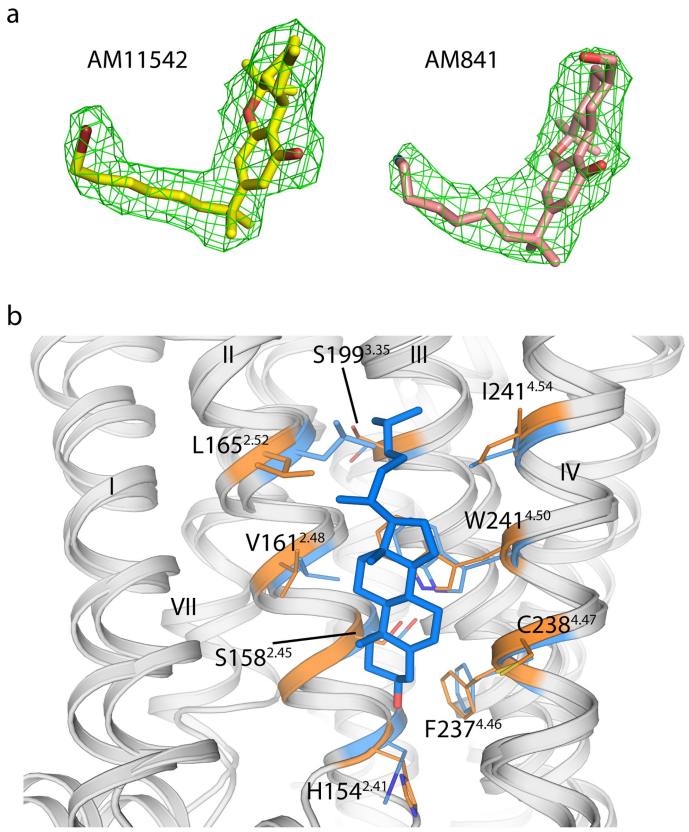

Extended Data Fig. 3 | Representative electron density of the CB_1 agonists-bound structures and cholesterol binding sites. a, The $|F_o|-|F_c|$ omit maps of AM11542 and AM841 contoured at 3.0σ at 2.80 Å and 2.95 Å, respectively. **b**, The cholesterol binding site in the CB_1–AM11542 structure (orange) with CB_1–AM6538 structure (blue) superposed.

a

Mutation	% + Cells	% WT surface	Primers for site-directed mutagenesis	
F177A	90	139	*forward*	CTTCATTGACGCCCACGTGTT
			reverse	CTGTAGACAAAAATGACACTCCCC
L193A	88	136	*forward*	TCTGTTCAAAGCGGGTGGGGT
			reverse	AACACGTTGCGGCTATCTTTGC
D213A	65	100	*forward*	ACAGCCATCGCCAGGTACAT
			reverse	GAGGAACAGGCTGCCCA
Y275F	76	117	*forward*	GATGAAACCTTCCTGATGTTC
			reverse	AATGTGTGGGAAAATGTCTG
Y275A	72	111	*forward*	GATGAAACCGCCCTGATGTTC
F379W	81	125	*forward*	GTGTGGGCATTCTGCAGT
			reverse	CGTCTTAATGAGCTTGTTCATC
F379A	76	117	*forward*	GTGGCTGCATTCTGCAGT
S383A	90	139	*forward*	TGCGCTATGCTCTGCCT
			reverse	GAATGCAAACACCGTCTTAATGAGC
T210A	65	94	*forward*	TCCTCGCAGCCATCGACAGG
			reverse	ACAGGCTGCCCACGGAGG
E273K	62	90	*forward*	CACATTGATAAAACCTACCTGATGT
			reverse	TGGGAAAATGTCTGAGCAAA
T283V	65	95	*forward*	GGTCGTCAGCGTACTGCTTC
			reverse	CCGATCCAGAACATCAGGTAGG
R340E	62	90	*forward*	ACATTGAGTTAGCCAAGACCC
			reverse	CCATGCGGGCTTGGT

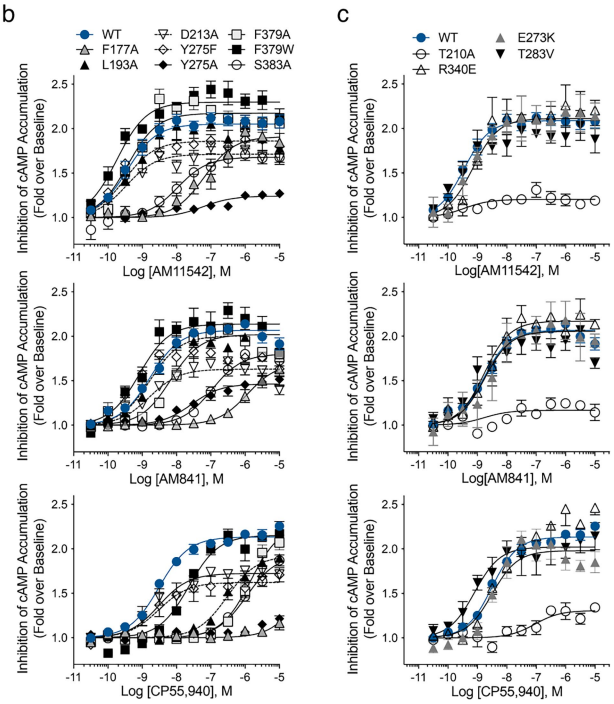

Extended Data Fig. 4 | Mutations of the CB_1 receptor and the effects on agonist-induced activity as assessed by the forskolin-stimulated accumulation of cAMP. a, Primers used to generate mutations in 3×HA–CB_1 and validation of cell-surface expression of wild-type and mutant CB_1 in CHO-K1 cell lines quantitative flow cytometry. **b**, Dose response studies of agonist (AM11542, AM841 and CP55,940) activity for each mutant compared to wild type (in blue filled circles) from Fig. 3c. **c**, Assessment of the effect of the individual point mutations that were made to stabilize the receptor, in absence of the flavodoxin insert, on receptor activity. All experiments were repeated at least three times, and error bars denote s.e.m. of duplicate measurements (parameters are in Extended Data Table 2).

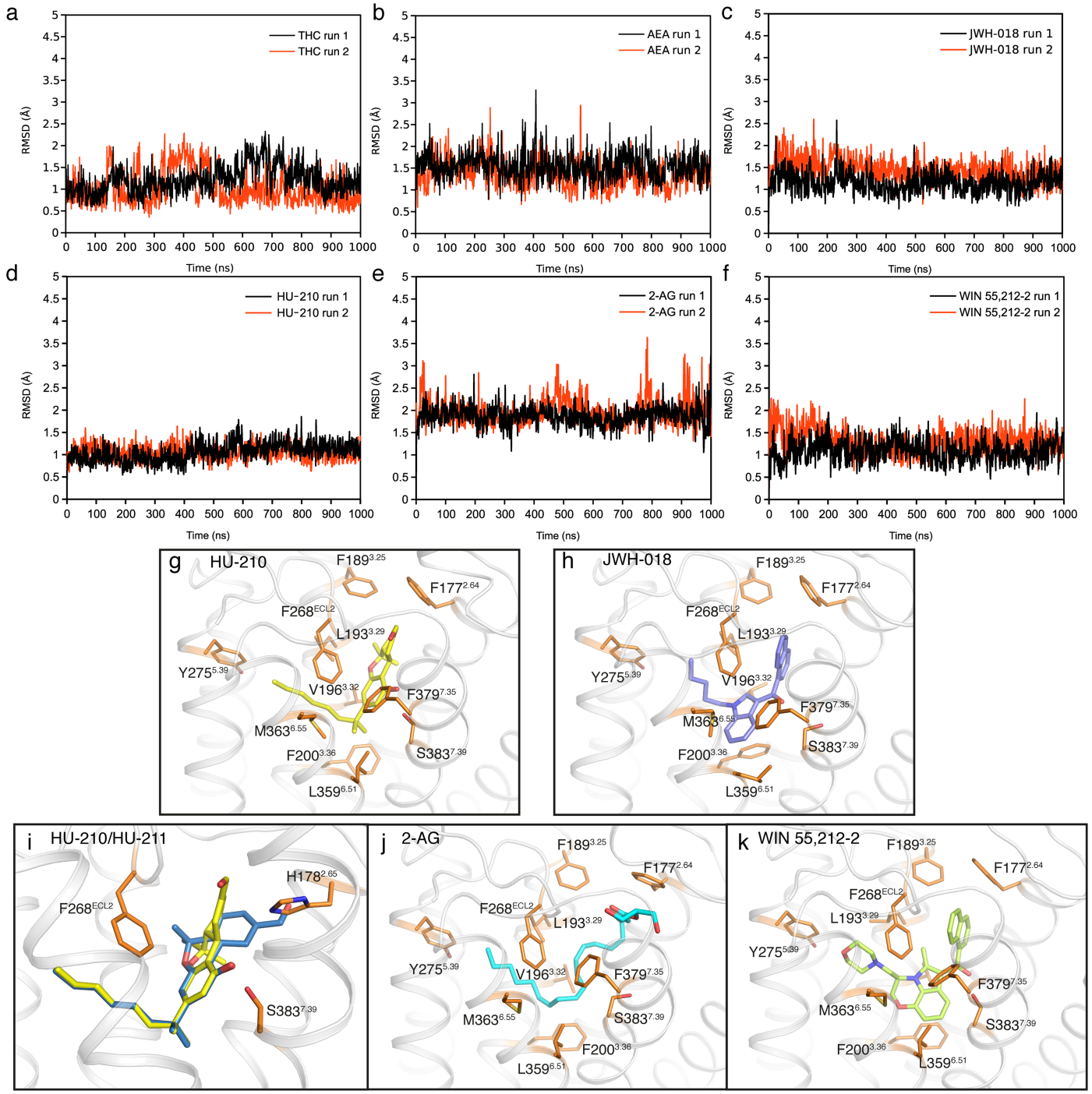

Extended Data Fig. 5 | Docking poses of different cannabinoid receptor agonists and MD validation. a–**f**, The r.m.s.d. values of ligand heavy atoms show that the docked poses are stable during the 1 μs molecular dynamics simulations: Δ^9-THC (**a**), AEA (**b**), JWH-018 (**c**), HU-210 (**d**), 2-AG (**e**), WIN 55,212-2 (**f**). **g**, **h**, **j**, **k**, The poses of HU-210 (**g**), JWH-018 (**h**), 2-AG (**j**) and WIN 55,212-2 (**k**) are shown. **i**, The superimposition of HU-210 (yellow sticks) and HU-211 (blue sticks) in the binding pocket. The binding pose of HU-210 explains why HU-211, the enantiomer of HU-210, failed to stimulate CB_1 because superimposed HU-211 on HU-210 shows severe clashes with $H178^{2.65}$ in CB_1.

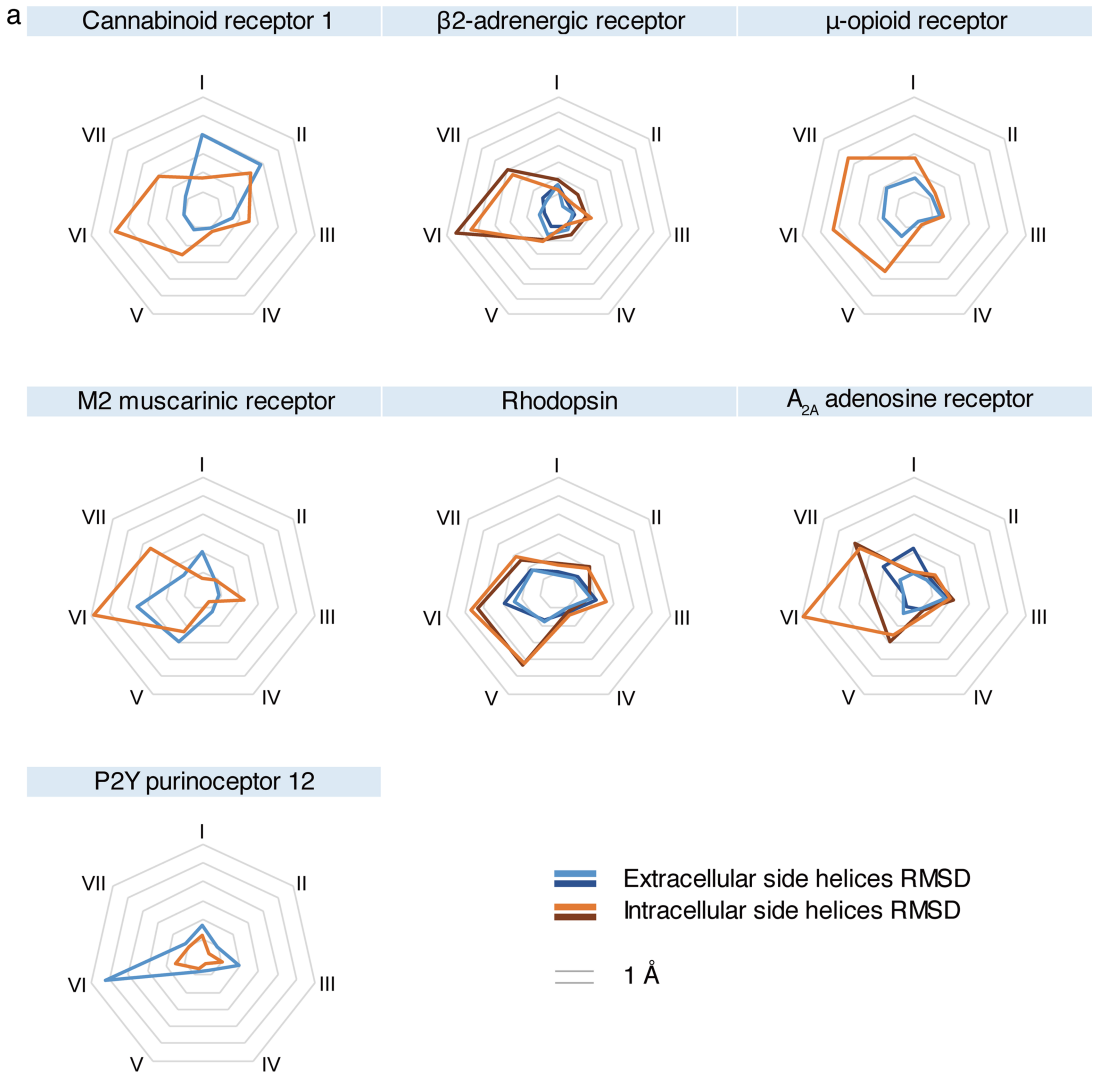

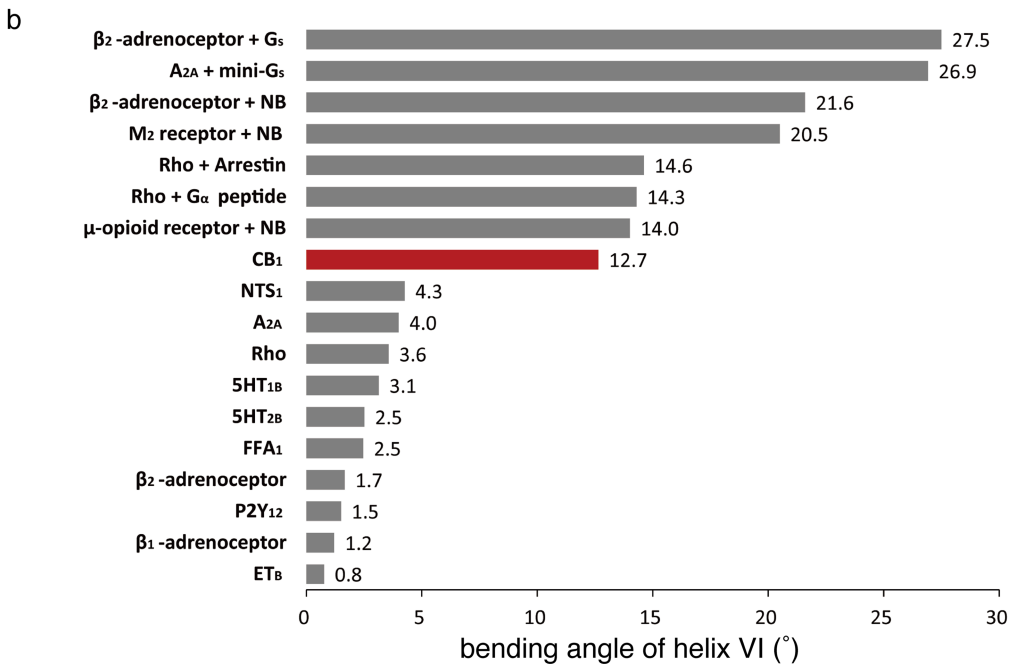

Extended Data Fig. 6 | See next page for caption.

Extended Data Fig. 6 | Structural conformation changes of solved agonist- and antagonist-bound class A GPCRs. a, The pattern of r.m.s.d. values of transmembrane helices between agonist- and antagonist-bound class A GPCR structures. The structures used for analysis are the same as described in Extended Data Table 3. **b**, Measurement of the degree of helix VI bending observed in class A GPCRs structures. All structures were superimposed onto inactive-state β_2-adrenergic receptor by UCSF Chimera. The direction of helices VI were defined by vectors $\boldsymbol{\eta_i}$ which starts from the centre of C_α of residues 6.45–6.48 to the centre of C_α of residues 6.29-30–6.32-33. The two vectors $\boldsymbol{\eta_o}$ and $\boldsymbol{\eta_1}$ of helices VI in the inactive-state and active-state β_2-adrenergic receptor were selected as reference to form a plane $\boldsymbol{\alpha}$. The vector $\boldsymbol{\eta_i}$ of helix VI of other structure was projected to the plane $\boldsymbol{\alpha}$ as a new vector $\boldsymbol{\eta_i'}$. The bending angle of each helix VI was then defined by the angle between $\boldsymbol{\eta_i'}$ and $\boldsymbol{\eta_o}$. The structures are: ET_B (PDB code 5GLH), β_1-adrenergic receptor (PDB code 2Y02), $P_{2Y}12$ (PDB code 4PXZ), β_2-adrenergic receptor (PDB code 3PDS), FFA1 (PDB code 4PHU), $5HT_{2B}$ (PDB code 4IB4), $5HT_{1B}$ (PDB code 4IAR), Rho (PDB code 2HPY), A_{2A} (PDB code 3QAK), NTS_1 (PDB code 4BUO), CB_1 (bound to AM11542; PDB code 5XRA), μ-opioid receptor + nanobody (NB) (PDB code 5C1M), Rho + NB (PDB code 2×72), Rho + arrestin (PDB code 4ZWJ), M2R + NB (PDB code 4MQS), β_2-adrenergic receptor + NB (PDB code 4LDL), A_{2A} + mini-G_s (PDB code 5G53), β_2-adrenergic receptor + G_s (PDB code 3SN6).

Extended Data Table 1 | Data collection and structure refinement statistics

	CB1-AM11542 (PDB: 5XRA)	CB1-AM841 (PDB: 5XR8)
Data collection		
Number of crystals	16	10
Space group	$P2_122_1$	$P2_122_1$
Cell dimensions		
a, *b*, *c* (Å)	66.05, 75.87, 138.90	66.83, 73.61, 139.64
Number of reflections measured	102213	84586
Number of unique reflections	16685	13367
Resolution (Å)[a]	37.91-2.80 (2.90-2.80)	49.48-2.95 (3.05-2.95)
$R_{merge,}$	0.101 (0.562)	0.081 (0.490)
Mean $I/\sigma(I)$	10.41 (2.07)	11.06 (1.97)
$CC_{1/2}$	1 (0.62)	1 (0.54)
Completeness (%)	93.50 (90.03)	88.18 (77.30)
Redundancy	6.1 (4.8)	6.3 (3.6)
Refinement		
Resolution (Å)	37.91-2.80	49.48-2.95
No. reflections	16669	13329
R_{work} / R_{free} (%)	23.4/25.2	25.5/27.4
No. atoms		
Protein	3311	3314
Ligand	28 (AM11542)	29 (AM841)
Lipid and other	122	66
Average B factors (Å^2)		
Wilson / Overall	79.6 / 90.0	110.0 / 130.7
CB_1	82.9	121.6
Flavodoxin	105.9	152.0
Ligand	62.4	93.3
Lipids and other	81.9	106.3
R.m.s. deviations		
Bond lengths (Å)	0.003	0.002
Bond angles (°)	0.732	0.484
Ramachandran Plot Statistics (%)		
Favored regions	97.88	96.02
Allowed regions	2.12	3.98
Disallowed regions	0	0

[a]Values in parentheses are for highest-resolution shell.

Extended Data Table 2 | Mutations analysis of changes in pEC_{50} and E_{max}

	AM11542			AM841			CP55,940		
CB1	pEC_{50}, M	E_{max} (Fold)	N	pEC50, M	E_{max} (Fold)	N	pEC50, M	E_{max} (Fold)	N
WT	9.5 ± 0.12	2.1 ± 0.03	18	8.7 ± 0.08	2.1 ± 0.02	18	8.5 ± 0.06	2.1 ± 0.02	10
F177A	7.1 ± 0.09****	1.9 ± 0.04	6	5.9 ± 0.14****	1.7 ± 0.08	6	4.7 ± 1.47****	1.4 ± 0.94	3
L193A	9.4 ± 0.20	2.0 ± 0.04	11	9.2 ± 0.20	1.7 ± 0.04	7	6.5 ± 0.09****	1.9 ± 0.04	4
D213A	9.6 ± 0.10	1.7 ± 0.02	3	9.0 ± 0.14	1.6 ± 0.03	3	8.6 ± 0.09	1.7 ± 0.02	3
Y275A	7.2 ± 0.20**	1.2 ± 0.02	6	7.5 ± 0.11****	1.5 ± 0.02	11	5.3 ± 0.45****	1.2 ± 0.09	8
Y275F	10.0 ± 0.14	1.8 ± 0.02	5	9.5 ± 0.16	1.8 ± 0.03	3	8.8 ± 0.24	1.6 ± 0.04	3
F379A	9.5 ± 0.15	2.2 ± 0.04	12	8.1 ± 0.11****	2.0 ± 0.04	8	5.9 ± 0.07****	2.3 ± 0.06	4
F379W	9.8 ± 0.13*	2.3 ± 0.03	3	9.2 ± 0.14*	2.1 ± 0.04	3	7.8 ± 0.08****	2.1 ± 0.03	3
S383A	8.1 ± 0.13****	1.7 ± 0.03	8	7.0 ± 0.10****	1.8 ± 0.03	7	6.0 ± 0.08****	1.9 ± 0.05	3
T210A	9.3 ± 0.42	1.2 ± 0.02	3	7.7 ± 0.40	1.2 ± 0.03	3	7.0 ± 0.30*	1.3 ± 0.04	3
E273K	9.2 ± 0.11	2.1 ± 0.03	3	8.6 ± 0.14	2.1 ± 0.04	3	8.6 ± 0.16	2.0 ± 0.05	3
T283V	9.7 ± 0.19	1.9 ± 0.04	3	9.2 ± 0.18*	1.9 ± 0.04	3	9.1 ± 0.20****	2.0 ± 0.05	3
R340E	9.1 ± 0.11	2.2 ± 0.03	3	8.6 ± 0.10	2.2 ± 0.03	3	8.2 ± 0.09	2.3 ± 0.04	3

Inhibition of forskolin-stimulated cAMP accumulation in wild-type and mutant CB_1 CHO cells. Data are mean pEC_{50} and E_{max} values±s.e.m. from fitting concentration–response data to nonlinear regression (3 parameter) analysis; $n \geq 3$ independent experiments performed in duplicate with the n shown in the table. Comparison to wild type with agonist treatment: *$P<0.05$, **$P<0.01$, ****$P<0.0001$ as determined by an extra sum-of-squares F-test using Prism 9.0. The last four mutations represent those appearing in the crystal structure CB_1 construct.

Extended Data Table 3 | Binding pocket volume comparison and r.m.s.d. analysis of solved representative agonist- and antagonist-bound pairs of seven class A GPCRs

GPCRs	Agonist-bound Structures	Binding Pocket Volume (Å^3)	Antagonist-bound Structures	Binding Pocket Volume (Å^3)	RMSD (Å) of transmembrane helices	
Cannabinoid receptor 1 (CB_1)	Agonist (PDB:5XRA)	383.5	Antagonist (PDB:5TGZ)	821.8	E	2.50
					I	3.07
β2-adrenergic receptor	Agonist (PDB:3SN6)	469.7	Inverse agonist (PDB:3NY8)	670.9	E	1.13
					I	3.40
	Agonist (PDB:4LDL)	670.9			E	1.19
					I	2.96
μ-opioid receptor	Agonist (PDB:5C1M)	576.6	Antagonist (PDB:4DKL)	586.5	E	1.49
					I	3.04
M_2 muscarinic receptor	Agonist (PDB:4MQS)	114.6	Antagonist (PDB:3UON)	320.7	E	1.99
					I	3.17
Rhodopsin	Agonist (PDB:2X72)	342.3	Antagonist (PDB:1U19)	214.7	E	1.72
					I	3.19
	Arrestin (PDB:4ZWJ)	373.8			E	1.56
					I	3.24
A_{2A} adenosine receptor	Agonist (PDB:3QAK)	445.2	Antagonist (PDB:4EIY)	461.0	E	1.58
					I	2.23
	Agonist (PDB:5G53)	288.8			E	1.12
					I	3.28
P2Y purinoceptor 12 ($P2Y_{12}$)	Agonist (PDB:4PXZ)	298.8	Antagonist (PDB:4NTJ)	392.7	E	2.13
					I	0.93

E: RMSD of extracellular side helices; I: RMSD of intracellular side helices.

nature portfolio

Corresponding author(s): Zhi-Jie Liu

Last updated by author(s): Jun 3, 2025

Reporting Summary

Nature Portfolio wishes to improve the reproducibility of the work that we publish. This form provides structure for consistency and transparency in reporting. For further information on Nature Portfolio policies, see our Editorial Policies and the Editorial Policy Checklist.

Statistics

For all statistical analyses, confirm that the following items are present in the figure legend, table legend, main text, or Methods section.

n/a	Confirmed	
☐	☒	The exact sample size (*n*) for each experimental group/condition, given as a discrete number and unit of measurement
☐	☒	A statement on whether measurements were taken from distinct samples or whether the same sample was measured repeatedly
☐	☒	The statistical test(s) used AND whether they are one- or two-sided *Only common tests should be described solely by name; describe more complex techniques in the Methods section.*
☒	☐	A description of all covariates tested
☒	☐	A description of any assumptions or corrections, such as tests of normality and adjustment for multiple comparisons
☐	☒	A full description of the statistical parameters including central tendency (e.g. means) or other basic estimates (e.g. regression coefficient) AND variation (e.g. standard deviation) or associated estimates of uncertainty (e.g. confidence intervals)
☐	☒	For null hypothesis testing, the test statistic (e.g. *F*, *t*, *r*) with confidence intervals, effect sizes, degrees of freedom and *P* value noted *Give P values as exact values whenever suitable.*
☒	☐	For Bayesian analysis, information on the choice of priors and Markov chain Monte Carlo settings
☒	☐	For hierarchical and complex designs, identification of the appropriate level for tests and full reporting of outcomes
☒	☐	Estimates of effect sizes (e.g. Cohen's *d*, Pearson's *r*), indicating how they were calculated

Our web collection on statistics for biologists contains articles on many of the points above.

Software and code

Policy information about availability of computer code

Data collection	X-ray diffraction data were collected at GM/CA-CAT beamline 23ID-B at the Advanced Photon Source (APS), Argonne National Laboratory IL, using an Eiger 16M detector (X-ray wavelength 1.0000 Å) and at beamline X06SA of the Swiss Light Source.
Data analysis	XDS, Phenix, Buster, COOT, Phaser, GraphPad Prism 7.0, Schrödinger Suite 2015-4, Glide 6.9, GROMACS 5.1.2, Amber 14, UCSF Chimera, Protein Preparation Wizard, Sitemap, BD FACSDiva version 8.0.1, FlowJo version 10.0.7,Prism software, v.9.0

For manuscripts utilizing custom algorithms or software that are central to the research but not yet described in published literature, software must be made available to editors and reviewers. We strongly encourage code deposition in a community repository (e.g. GitHub). See the Nature Portfolio guidelines for submitting code & software for further information.

Data

Policy information about availability of data

All manuscripts must include a data availability statement. This statement should provide the following information, where applicable:

- Accession codes, unique identifiers, or web links for publicly available datasets
- A description of any restrictions on data availability
- For clinical datasets or third party data, please ensure that the statement adheres to our policy

Atomic coordinates and structures have been deposited in the Protein Data Bank (PDB) with accession codes 5XRA (CB1–AM11542) and 5XR8 (CB1–AM841). Source data are provided with this paper.

Research involving human participants, their data, or biological material

Policy information about studies with human participants or human data. See also policy information about sex, gender (identity/presentation), and sexual orientation and race, ethnicity and racism.

Reporting on sex and gender	n/a
Reporting on race, ethnicity, or other socially relevant groupings	n/a
Population characteristics	n/a
Recruitment	n/a
Ethics oversight	n/a

Note that full information on the approval of the study protocol must also be provided in the manuscript.

Field-specific reporting

Please select the one below that is the best fit for your research. If you are not sure, read the appropriate sections before making your selection.

☒ Life sciences ☐ Behavioural & social sciences ☐ Ecological, evolutionary & environmental sciences

For a reference copy of the document with all sections, see nature.com/documents/nr-reporting-summary-flat.pdf

Life sciences study design

All studies must disclose on these points even when the disclosure is negative.

Sample size	XDS was used for integrating and scaling data from the 16 crystals for the CB1–AM11542 complex and 10 crystals for the CB1–AM841 complex. For functional assays, at least three biologically independent experiments were performed as depicted in related Figure legends.
Data exclusions	No data were excluded from the analysis.
Replication	At least 2 individual researchers replicated the pharmacology studies, in some cases three individuals.
Randomization	There was no randomization applied.
Blinding	There was no blinding applied as the results were not subjective.

Reporting for specific materials, systems and methods

We require information from authors about some types of materials, experimental systems and methods used in many studies. Here, indicate whether each material, system or method listed is relevant to your study. If you are not sure if a list item applies to your research, read the appropriate section before selecting a response.

Materials & experimental systems

n/a	Involved in the study
☐	☒ Antibodies
☐	☒ Eukaryotic cell lines
☒	☐ Palaeontology and archaeology
☒	☐ Animals and other organisms
☒	☐ Clinical data
☒	☐ Dual use research of concern
☒	☐ Plants

Methods

n/a	Involved in the study
☒	☐ ChIP-seq
☐	☒ Flow cytometry
☒	☐ MRI-based neuroimaging

Antibodies

Antibodies used	Dy-light 488 anti-HA antibody from Life Technologies; 26183-D488 cat. number

Validation	This antibody only recognizes the HA-tag as confirmed by lack of staining in cells that did not undergo transfection with an HA-tagged receptor.

Eukaryotic cell lines

Policy information about cell lines and Sex and Gender in Research

Cell line source(s)	CHO-K1 from ATCC. Female as these are Chinese Hamster Ovary cells.
Authentication	ATCC authentification
Mycoplasma contamination	Cells are tested monthly for mycoplasma
Commonly misidentified lines (See ICLAC register)	n/a

Plants

Seed stocks	n/a
Novel plant genotypes	n/a
Authentication	n/a

Flow Cytometry

Plots

Confirm that:

☐ The axis labels state the marker and fluorochrome used (e.g. CD4-FITC).

☐ The axis scales are clearly visible. Include numbers along axes only for bottom left plot of group (a 'group' is an analysis of identical markers).

☐ All plots are contour plots with outliers or pseudocolor plots.

☐ A numerical value for number of cells or percentage (with statistics) is provided.

Methodology

Sample preparation	Following transfection with HA-tagged CB1 mutants, CHO-K1 cells were subjected to flow cytometry on the next day to isolate a population of cells that have the N-terminal HA tag available for antibody binding. These cells were then grown under antibiotic selection and cell surface expression was confirmed by confocal microscopy. In some cases where expression was not robust, the lines were subjected to another round of flow cytometry to enrich the population of expressing cells. The approach was used to quickly generate a cell line, not to provide data for analysis and no figure is presented.
Instrument	FACS AriaIII
Software	Aria III standard software
Cell population abundance	Generally, 50,000 cells were screened at a time.
Gating strategy	A gating strategy was used to identify and select cells that expressed the HA tag.

☐ Tick this box to confirm that a figure exemplifying the gating strategy is provided in the Supplementary Information.